The HST/ACS Coma Cluster Survey

Hoyos, Carlos; den Brok, Mark; Verdoes Kleijn, Gijs; Carter, David; Balcells, Marc; Guzmán, Rafael; Peletier, Reynier; Ferguson, Henry C.; Goudfrooij, Paul; Graham, Alister W.

Published in:
Monthly Notices of the Royal Astronomical Society

DOI:
10.1111/j.1365-2966.2010.17855.x

Publication date:
2011

Monthly Notices
of the
ROYAL ASTRONOMICAL SOCIETY

Mon. Not. R. Astron. Soc. **411,** 2439–2460 (2011) doi:10.1111/j.1365-2966.2010.17855.x

The *HST*/ACS Coma Cluster Survey – III. Structural parameters of galaxies using single Sérsic fits⋆

Carlos Hoyos,[1,2,3]† Mark den Brok,[4] Gijs Verdoes Kleijn,[4] David Carter,[5] Marc Balcells,[6,7] Rafael Guzmán,[1] Reynier Peletier,[4] Henry C. Ferguson,[8] Paul Goudfrooij,[8] Alister W. Graham,[9] Derek Hammer,[10] Arna M. Karick,[5] John R. Lucey,[11] Ana Matković,[8,12] David Merritt,[13] Mustapha Mouhcine[5] and Edwin Valentijn[4]

[1]*Department of Astronomy, University of Florida, PO Box 112055, Gainesville, FL 32611, USA*
[2]*Departamento de Física Teórica, Facultad de Ciencias, Universidad Autónoma de Madrid, Cantoblanco, 28049 Madrid, Spain*
[3]*School of Physics and Astronomy, The University of Nottingham, University Park, Nottingham NG7 2RD*
[4]*Kapteyn Astronomical Institute, University of Groningen, PO Box 800, 9700 AV Groningen, the Netherlands*
[5]*Astrophysics Research Institute, Liverpool John Moores University, Twelve Quays House, Egerton Wharf, Birkenhead CH41 1LD*
[6]*Instituto de Astrofísica de Canarias, C/Vía Lactea s/n, 38200 La Laguna, Tenerife, Spain*
[7]*Isaac Newton Group of Telescopes, Apartado de Correos 321, E-38700 Santa Cruz de la Palma, Canary Islands, Spain*
[8]*Space Telescope Science Institute, 3700 San Martin Drive, Baltimore, MD 21218, USA*
[9]*Centre for Astrophysics and Supercomputing, Swinburne University of Technology, PO Box 218, Hawthorn, VIC 3122, Australia*
[10]*Department of Physics and Astronomy, Johns Hopkins University, 3400 North Charles Street, Baltimore, MD 21218, USA*
[11]*Department of Physics, Durham University, South Road, Durham DH1 3LE*
[12]*Astronomy and Astrophysics, Pennsylvania State University, 525 Davey Lab, University Park, PA 16802, USA*
[13]*Department of Physics and Center for Computational Relativity and Gravitation, Rochester Institute of Technology, Rochester, NY 14623, USA*

Accepted 2010 October 13. Received 2010 October 12; in original form 2010 September 22

ABSTRACT

We present a catalogue of structural parameters for 8814 galaxies in the 25 fields of the *Hubble Space Telescope*/ACS Coma Treasury Survey. Parameters from Sérsic fits to the two-dimensional surface brightness distributions are given for all galaxies from our published Coma photometric catalogue with mean effective surface brightness brighter than 26.0 mag arcsec^{-2} and brighter than 24.5 mag (equivalent to absolute magnitude −10.5), as given by the fits, all in $F814W$(AB). The sample comprises a mixture of Coma members and background objects; 424 galaxies have redshifts and of these 163 are confirmed members. The fits were carried out using both the GIM2D and GALFIT codes. We provide the following parameters: galaxy ID, RA, Dec., the total corrected automatic magnitude from the photometric catalogue, the total magnitude of the model ($F814W_{\rm AB}$), the geometric mean effective radius $R_{\rm e}$, the mean surface brightness within the effective radius $\langle\mu\rangle_{\rm e}$, the Sérsic index n, the ellipticity and the source position angle. The selection limits of the catalogue and the errors listed for the Sérsic parameters come from extensive simulations of the fitting process using synthetic galaxy models. The agreement between GIM2D and GALFIT parameters is sensitive to details of the fitting procedure; for the settings employed here the agreement is excellent over the range of parameters covered in the catalogue. We define and present two goodness-of-fit indices which quantify the degree to which the image can be approximated by a Sérsic model with concentric, coaxial elliptical isophotes; such indices may be used to objectively select galaxies with more complex structures such as bulge–disc, bars or nuclear components.

We make the catalogue available in electronic format at ASTRO-WISE and MAST.

⋆Based on observations made with the NASA/ESA *Hubble Space Telescope*, obtained at the Space Telescope Science Institute, which is operated by the Association of Universities for Research in Astronomy, Inc. under NASA contract NAS 5-26555. These observations are associated with programme GO10861.
†E-mail: dxc@astro.livjm.ac.uk

Key words: galaxies: clusters: individual: Coma – galaxies: dwarf – galaxies: elliptical and lenticular, cD – galaxies: evolution – galaxies: fundamental parameters.

1 INTRODUCTION

Surface brightness distributions are a vital tool in our understanding of galaxies. Since the pioneering work of Reynolds (1913) and Hubble (1930) on elliptical galaxies, it has become common to fit the radial surface brightness distributions to functions having a small number of parameters, which include a scalelength, a characteristic surface brightness and one or two further parameters which describe the structure of the surface brightness profile. The most commonly used fitting function is that of Sérsic (1963, 1968), whose function includes as special cases both the $R^{1/4}$ law of de Vaucouleurs (1948) and the exponential surface brightness distribution which is characteristic of disc galaxies (Patterson 1940; de Vaucouleurs 1957, 1959; Freeman 1970):

$$I(R) = I_{\rm e}\ \exp\{-b\ \left[(R/R_{\rm e})^{1/n} - 1\right]\}, \quad (1)$$

where $I(R)$ is the specific intensity at distance R from the centre, $R_{\rm e}$ is the radius enclosing half the galaxy light, $I_{\rm e}$ is the specific intensity at $R_{\rm e}$, n is the Sérsic index or concentration index (Trujillo, Graham & Caon 2001) and $b \approx 1.9992 \times n - 0.3271$ (Capaccioli 1989).

The Sérsic function provides a good model for ellipticals, giants showing values of $n \geqslant 4$, intermediate luminosity ellipticals $n \approx 2$–4 and dwarfs $n \approx 1$–2 (Caon, Capaccioli & D'Onofrio 1993; Graham et al. 1996; Graham & Guzmán 2003). Bulges of disc galaxies are also well fitted by the Sérsic model (Andredakis, Peletier & Balcells 1995) with indices $n \approx 0.5$–4 (Balcells, Graham & Peletier 2007b; Graham & Worley 2008). For disc galaxies, pure Sérsic fits often yield poor approximations to the entire galaxy surface brightness distribution, due to the presence of bulges, bars, spirals, outer disc truncations (e.g. van der Kruit & Searle 1981a, van der Kruit & Searle 1b) and anti-truncations (Erwin, Beckman & Pohlen 2005). However, classifying galaxies into early ($n > 2.5$) and late ($n < 2.5$) types on the basis of single Sérsic fits to the entire galaxy has become standard practice (e.g. van der Wel et al. 2008), especially in samples with limited image depth and spatial resolution which prevent more complex modelling. This practice fails when the samples include lower luminosity dwarf elliptical galaxies. The reliability of such fits may be calibrated by performing single Sérsic fits to nearby, well-resolved galaxies. Needed for the interpretation of such single Sérsic fits is a parameter that quantifies the degree to which the true surface brightness distribution deviates from the Sérsic model.

The *Hubble Space Telescope* (*HST*)/ACS Treasury Survey of the Coma cluster was presented in Carter et al. (2008, Paper I). Although the survey was originally planned to cover 740 arcmin^2 of the Coma cluster field, the final areal coverage is 274 arcmin^2 in the *F*475*W* and *F*814*W* bands, mostly in the core region, owing to the ACS failure in 2007 January. Still, with the exquisite quality and depth of the imaging and the large number of spectroscopic redshifts known for galaxies in this field (Colless & Dunn 1996; Mobasher et al. 2001; Marzke et al., in preparation; Chiboucas et al. 2010a), this survey allows studies of the structure of large samples of cluster members to an unprecedented depth. The photometric catalogue from the *HST*/ACS images was presented in Hammer et al. (2010, Paper II; see Section 2).

This paper presents a structural analysis of sources selected from a structural analysis of the sources from the Paper II photometric catalogue, based on two-dimensional single Sérsic fits. Of the ∼75 000 objects in that catalogue, we provide Sérsic parameters for 8814 galaxies that are located both inside the cluster and in the background; the selection function is explained in Section 6.1. We present standard Sérsic parameters as well as two goodness-of-fit indices, that provide a quantitative measure of the degree to which the galaxy surface brightness distribution deviates from a Sérsic model with concentric, co-axial elliptical isophotes (Section 5). These indices can be used to identify those galaxy images which allow for additional components, such as outer discs, nuclear components or bars. Given the complexity of the structural analysis process, we focus this paper on the presentation of the analysis techniques and of the catalogue. We defer scientific analysis to future papers. The structural parameters presented here can be used

(i) to study the cosmological evolution of galaxy sizes and shapes by using the Coma cluster as a local reference sample;

(ii) to quantify the faint end of global scaling relations, such as size–surface brightness diagrams and the Fundamental Plane, revealing how dwarf elliptical galaxies do or do not unite with brighter ellipticals;

(iii) to study the correlation between the structural parameters and the photometric masses of elliptical and lenticular galaxies, which could be used in cluster membership studies (Trentham et al., in preparation).

Our results in Coma can be compared with the lower density Virgo and Fornax cluster environments where targeted *HST*/ACS surveys provide structural information at higher physical resolution for smaller samples of galaxies (Ferrarese et al. 2006; Côté et al. 2007). The Coma data set may be also used in conjunction with *HST* surveys at higher redshift to study the evolution of the structural properties of galaxies. STAGES (Gray et al. 2009) is a survey of the supercluster Abell 901/2 at a redshift of 0.165. Amongst an extensive multiwavelength data set, ACS images have been used for Sérsic fits to a large sample of galaxies in the STAGES region. GEMS (Rix et al. 2004) is an ACS survey of a 900-arcmin^2 region within the Extended *Chandra Deep Field*-South region. Although it is a field rather than cluster survey, it provides a useful evolution benchmark at redshifts approaching $z = 1$. *HST* has been used to study the structural properties of galaxies in higher redshift clusters, where there is a suggestion of size evolution by up to a factor of 4 (e.g. Trujillo et al. 2006; Strazzullo et al. 2010).

There are currently a number of codes capable of performing two-dimensional Sérsic model fits to the surface brightness distribution of galaxies. Two extensively used are GIM2D (Simard et al. 2002) and GALFIT (Peng et al. 2002). Both codes work by minimizing a merit function, and produce similar outputs, but their inner workings differ in a number of ways, such as the minimization technique: GIM2D uses the Metropolis algorithm, whereas GALFIT uses the Levenberg–Marquardt algorithm. GALFIT offers practical advantages, such as higher execution speed and the ability to simultaneously fit several targets. But because each code has its own merits, we carried out the fits using both codes, and present both results. In order not to bias the comparison, two teams worked largely independently, one with GIM2D, and another with GALFIT. While some details differ, e.g. in the parameter ranges explored in the Monte Carlo simulations, there

was enough coordination to ensure the results would be comparable to each other. We show in Section 7 that the agreement is very good.

GIM2D and GALFIT were compared by Häussler et al. (2007), who concluded that both could produce similar results, but warned against a systematic underestimate of both the total luminosity and effective radius of the GIM2D output for lower surface brightness sources. We were able to reproduce their findings; in Section 3 we present an approach which successfully overcomes these biases.

The paper is structured as follows. Section 2 describes the input data from which our catalogue is derived. Sections 3 and 4 describe how the GIM2D and GALFIT analysis runs on the Coma data were set up. Section 5 introduces two additional parameters calculated from the residuals of the data from the models which describe how well the Sérsic model fits the data. Section 6 presents the final structural parameters catalogue and the criteria for inclusion in the catalogue. Section 7 presents a comparison between the results obtained with two codes on the Coma data. In Section 8, we present our conclusions and describe the next steps in the analysis of the galaxies and their surface brightness distributions. In Appendix A, we compare our results with those of Häussler et al. (2007).

Throughout the paper, we assume the distance to Coma of 100 Mpc, corresponding to a distance modulus of $m - M = 35.0$ (see Paper I). All magnitudes are in the AB system. In this paper, with a few exceptions, we express the surface brightness in terms of the mean effective surface brightness $\langle\mu\rangle_e$, i.e. the mean surface brightness enclosed within R_e. Graham & Driver (2005) show that the relationship between $\langle\mu\rangle_e$ and the effective surface brightness μ_e (surface brightness at R_e) is given by

$$\langle\mu\rangle_e = \mu_e - 2.5\log[f(n)], \tag{2}$$

where

$$f(n) = \frac{ne^b}{b^{2n}}\int_0^\infty e^{-x}x^{2n-1}dx = \frac{ne^b}{b^{2n}}\Gamma(2n), \tag{3}$$

and $\Gamma(2n)$ is the complete gamma function. Total magnitude m is related to $\langle\mu\rangle_e$ by the simple relation:

$$m = \langle\mu\rangle_e - 2.5\log(2\pi R_e^2). \tag{4}$$

2 DATA

2.1 *HST*/ACS images

The survey design and reduction of the images are described in detail in Paper I, so only a summary will be provided here. The observations (program GO 10861) were taken between 2006 November and 2007 January with the *HST*/ACS camera ($2 \times 4096 \times 2048$ pixels, 0.05 arcsec pixel^{-1}, 3-arcsec interchip gap). A total of 25 visits were completed before the failure of ACS. Most fields (19/25) are located within 0.5 Mpc of the cluster centre (the full list of survey fields is given in table 2 of Paper I). The remaining six fields are in the south-west extension of Coma. Two *HST* orbits were devoted to each pointing. A four-position dither pattern was used for each of the *F*475*W* and *F*814*W* images, with total integration times of 2560 and 1400 s, respectively. The dither pattern allowed us to fill the ACS interchip gap, albeit with lower signal-to-noise ratio (S/N). Total exposure times were lower for some visits due to dither positions that failed to acquire guide stars. Final exposure times are given in table 5 of Paper I.

Data reduction was carried out with a dedicated pipeline. It included the combination of individual images with the MULTIDRIZZLE software (Koekemoer et al. 2003), which yields combined images resampled on to a rectified (but original sky orientation) output frame with 0.0495 arcsec pixel^{-1}. Cosmic rays were removed during the multidrizzle process and also using LACOSMIC (van Dokkum 2001). These processed images, together with an initial source catalogue, comprised the first data release (DR1), 2008 August.[1]

2.2 Catalogues of the Coma Data Release 2

The second data release (DR2), available at the same websites as DR1, includes improvements in alignment between *F*814*W* and *F*475*W* images, better astrometry, aperture corrections to the SEXTRACTOR photometry and photometry of sources that project on to large galaxies. Details of the data processing and description of the DR2 photometric catalogues, including the SEXTRACTOR (version 2.5; Bertin & Arnouts 1996) configuration parameters employed in the catalogue generation, are given in Paper II. The DR2 catalogues contain ∼73 000 sources. Based on Monte Carlo simulations, the 80 per cent completeness limit for point sources in the DR2 catalogues is 27.8 mag in *F*475*W* and 26.8 mag in *F*814*W*.

The DR2 images and catalogues are the basis for the structural analysis done with GALFIT, whereas GIM2D fitting was performed on the DR1 images and catalogue. This difference represents no problems. Comparison of the SEXTRACTOR catalogues from the two releases shows that 99 per cent of the detected sources match, with 75 per cent of the additional catalogue objects in DR1 being in visit 03, which lacked two of the four dither positions. These additional objects would in any case be fainter and smaller than the catalogue limits of the current paper (Section 6.1). We refer to the DR2 catalogue as the 'photometric catalogue' throughout this paper.

2.3 PSF

The point spread function (PSF) is a key ingredient of any S/N weighted analysis of the morphological and structural properties of galaxies. The PSF of the Wide Field Channel (WFC) of the ACS has been extensively studied. Jee et al. (2007) and Rhodes et al. (2007) offer different suites for creating ACS PSFs for a variety of observing conditions. The *HST* Instrument Science Report 0306 (Krist 2003) presents a detailed study of the variation of the PSF across the WFC chips. The PSF of the WFC depends both on time and position on the chip. The TINYTIM program (Krist 1993) takes advantage of this empirical knowledge, and creates artificial PSFs for a large variety of observing conditions and *HST* instruments.

We created a grid of ACS PSFs using TINYTIM. These were then combined using the code DRIZZLYTIM, by Luc Simard, kindly made available to us by the author.

DRIZZLYTIM calculates the location of the original PSFs in the calibrated flat-fielded individual exposures, using the same multidrizzling parameters and shift file as used to produce the science images. DRIZZLYTIM then invokes TINYTIM to create the required PSFs in the calibrated, flat-fielded set of coordinates. The PSFs are created with an oversampling of 5, and assuming a 6500 K blackbody as a representation of the object spectrum. This is appropriate for the E and S0 galaxies in our sample. DRIZZLYTIM then places these PSFs into blank frames, with the same size and header parameters as those of the real flat-fielded individual exposures. These frames are then co-added, using again the same multidrizzle parameters as those used to manufacture the final science images. The final

[1] MAST (archive.stsci.edu/prepds/coma/) and Astro-WISE (www.astro-wise.org/projects/COMALS/)

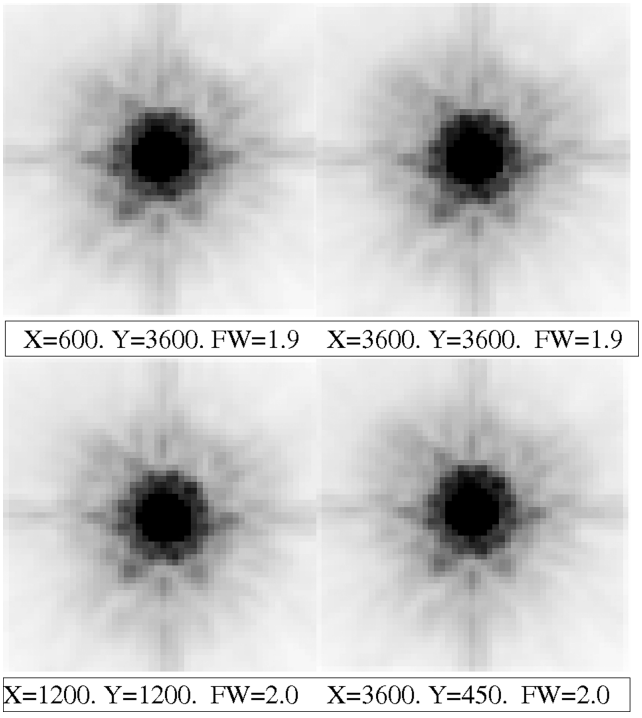

Figure 1. Four examples of the PSFs created by DrizzlyTim. These PSFs were used by gim2d and galfit to fit the real sources in the science images. The image in each panel is 50 pixels (2.0 arcsec) square.

step is to apply the Charge Diffusion Kernel to these newly created PSFs in the calibrated, geometrical distortion corrected images. We followed this process to create a grid of PSFs with the sampling of the original images. One PSF was created every 150 pixels in x and y directions, and the PSF imagelets created were 31 pixels on a side. The typical full width at half-maximum (FWHM) of the PSFs created was 2.0 pixels, with at most a 20 per cent variation across the field. As the time period over which the images were obtained was short, we did not allow for temporal variation of the PSF. When fitting real galaxies, both gim2d and galfit were instructed to use the nearest PSF to that object.

Fig. 1 shows a set of DrizzlyTim PSFs, with their respective FWHM.

3 gim2d FITTING

This section describes the gim2d set-up used to fit the surface brightness distributions of the detected galaxies. As will also be done in Section 4 for galfit, we build upon the experience of the GEMS collaboration who analyse galaxies from *HST*/ACS imaging, and perform extensive simulations to compare systematics in gim2d and galfit (Häussler et al. 2007). From our own analysis of the Häussler et al. paper, shown in Appendix A, we conclude that mask creation is critical for gim2d, and we present a new prescription for creating the masks that gim2d requires for object detection and fitting. In addition, this section presents Monte Carlo simulations used to assign statistical errors to the gim2d best-fitting parameters.

3.1 Object masks for gim2d

Our own simulations, and those of Häussler et al. (2007), show that gim2d can miss a substantial fraction of light from faint sources (a comparison of our simulations to those of Häussler et al. is given in Appendix A). Our analysis concludes that this problem originates in the use of SExtractor segmentation masks as input for gim2d. When gim2d is instructed to infer its initial guesses from SExtractor magnitude and size parameters (DOINIT = YES), and is allowed to refine the sky level estimate obtained from SExtractor (DOBKG = YES), the use of SExtractor segmentation masks leads to systematically fainter and smaller solutions. Setting DOBKG and DOINIT to NO (i.e. sky background fixed from SExtractor, and initial estimates of other parameters taken from the parameter file *gal.mdpar*) fixes the systematic error in total magnitude and R_e, but at the expense of an increase scatter in the solutions, and a dramatic increase in the convergence time. When DOBKG and DOINIT are both set to YES, gim2d is left free to automatically decide which section of the global parameter space to explore. gim2d does this using the mask image it has been provided. It first estimates the sky using the pixels designated as sky pixels in the mask image that lie a fixed number (which we set to 10) of pixels away from the target mask. It then subtracts this estimate of the sky value from the input image, and derives initial estimates of the total flux, inclination angle, ellipticity and effective radius. In this important step, gim2d calculates the total flux and the effective radius of the target using pixels which, according to the mask it has been given, belong to the ISOAREA of that object. gim2d will then explore the range in parameter space from 0 counts to twice the sky subtracted flux within the mask, and from 0 pixels to twice the effective radius of the set of pixels within the mask. This factor of 2 is hard coded into gim2d and cannot be tweaked.

Therefore if gim2d is set with both DOBKG = YES, DOINIT = YES and fed with a segmentation image from SExtractor, it will only explore magnitudes between (MAG_ISO −0.75) and infinity. However, the SExtractor simulations presented in Paper II show that for the fainter sources the real magnitudes can be off from MAG_AUTO by up to 2 mag. A very similar statement could be made for the effective radius. In this case, the range in linear size explored is from 0 pixel to twice the gim2d initial estimate, which is built from the two-dimensional Kron radius. This effective radius estimate was found to be different from the true effective radius by up to a factor of 5 for the less luminous sources.

This clearly indicates that the masks gim2d is provided have to be enlarged, if they are to be a faithful representation of the real extent of the targets. Instead of using the standard segmentation image created by SExtractor, we build a customized mask for each object, using the information from the SExtractor catalogue for the whole frame and the knowledge of the noise properties of the images. This mask image is constructed separately for each particular object, since gim2d treats target and background sources differently. Any given object is represented by one aperture when acting as the target, and is represented by another smaller aperture when being considered a background source possibly affecting the fit of a different object. The properties of the proposed masks, together with the practical steps required to create them, are summarized in Appendix B.

Fig. 2 shows four examples of galaxies, together with their associated masks. Black pixels belong to the target object, white pixels belong to other sources and grey pixels are sky. The first object is a low surface brightness source that was however detected by SExtractor. The second and fourth objects are spiral galaxies. In all cases, the field of views are given in the image insets. The Kron-like apertures which were adopted for the targets, presented as black pixels on the mask images, are clearly more extended than the visible flux from the target galaxy, and are typically much larger than

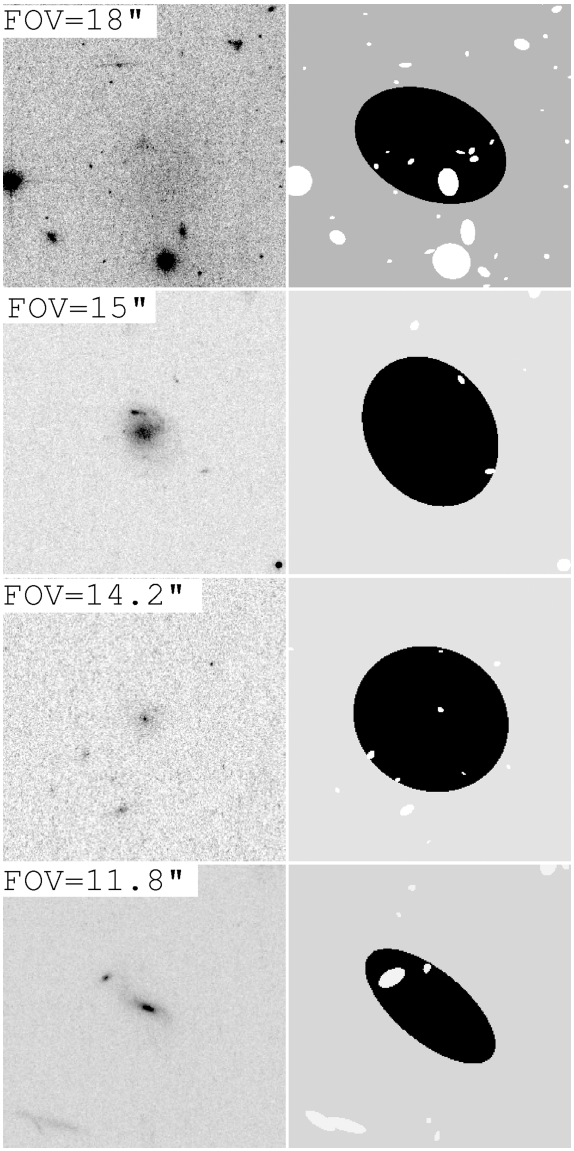

Figure 2. Examples of the masks used by GIM2D. The 'Kron-like' apertures devised for the four target objects are much larger than the apertures of their neighbouring sources, which have an area equal to their ISOAREA_IMAGE.

the isophotal apertures used for neighbouring objects which are shown as white pixels. The apertures for the background sources can overlap the aperture of the target object, which is not possible when using the segmentation images produced by SEXTRACTOR, when the background objects can potentially interfere with the ability of GIM2D to measure regions outside the ISOAREA_IMAGE of the target.

3.2 Noise model

A simple noise model is used for the fits. When GIM2D is not given a specific noise image, it builds an internal weight map based upon the rms of the background ($\sigma_{\rm bkg}$) and the effective gain, which is a function of the effective exposure time of the science frames. This noise model is a translation of the usual CCD uncertainty equation. In our case, $\sigma_{\rm bkg}$ is taken directly from the SEXTRACTOR catalogue, although it is later recalculated by GIM2D in most cases. The effective exposure time is read from the header of the *HST*/ACS frames.

With DOBKG set to YES, GIM2D refines the sky value given by SEXTRACTOR, and obtains a better estimate of $\sigma_{\rm bkg}$. This is then used to construct the internal weight map. The sky pixels involved in this calculation were at least 10 pixels away from those pixels determined to belong to the target object. The refined sky value is the median value of at least 30 pixels, applying a 5σ clipping thresholding scheme. The rms of the background obtained by GIM2D in this way is generally in excellent agreement with the $\sigma_{\rm bkg}$ initially estimated by SEXTRACTOR, both in the mean and variance. In cases where insufficient numbers of pixels were available to estimate the background rms inside the imagelet (owing to crowded fields), GIM2D defaulted to the user-supplied rms that was estimated by SExtractor.

3.3 Final GIM2D configuration

DOINIT was set to NO. The lower limit of the total flux was set to 0, while the upper limit was set to 10 times the automatic aperture flux. The bulge-to-total fraction was set to 1. The effective radius ranged from 0.0 to 10.0 times the effective radius estimate obtained for a pure Sérsic model of $n = 2.25$ of the same MUOBS and FLUX_RADIUS. The ellipticity and position angle were allowed to search their whole ranges. The X and Y drifts were permitted to range from -10 to 10 pixels, and the residual sky value was allowed to go from -0.25 to 0.25. The Sérsic index n was allowed to range from 0.25 to 10.0. Thus, each object had an individualized GIM2D configuration file leading to all objects being fit by a single Sérsic profile. The Metropolis temperatures are adequate for the explored ranges, and expected typical changes in each iteration. In all cases, saturated pixels were rejected from the fits. The Metropolis algorithm is given 400 iterations to cool off after achieving convergence (see Simard et al. 2002 for more technical detail).

3.4 Errors on the parameters and depth of the survey

Although GIM2D produces, together with its results, a set of confidence intervals for the fitted parameters, the error estimates represent only the scale upon which the figure-of-merit that GIM2D uses is expected to vary. Therefore, these confidence intervals merely reflect how constrained the fit is. A more realistic and meaningful error analysis needs to investigate the extent to which the minimum of the Figure-of-Merit can drift in its parameter space.

A modest number of Monte Carlo GIM2D simulations was run. The purpose of these simulations is twofold. The first is to be able to ascribe realistic statistical errors to the fits produced by GIM2D. The second purpose is to assess the surface brightness limit beyond which it will not be possible to recover reliable structural parameters.

10 000 model images were created using GALIMAGE within IRAF.FUZZY. In this step, a Moffat (1969) PSF representative of the average properties of several non-saturated stars was used to degrade the galaxy models. MKNOISE was then used to add appropriate Poissonian noise to this model. This blurred image was then added to a real ACS image which therefore provides the readout noise, and the bulk of the error correlation that is typical of ACS drizzled images. The selected canvas images correspond to visits 1, 15, 78 and 90 (see Paper I). SEXTRACTOR and GIM2D were run, with the same parameters, weight images and flag images as those used to create the SEXTRACTOR catalogue and the same experimental set-up described above, using the Moffat PSF as the convolution kernel.

The mean effective surface brightnesses of the models ran from 19.0 to 27.0, with effective radii distributed randomly in $\log R_{\rm e}$

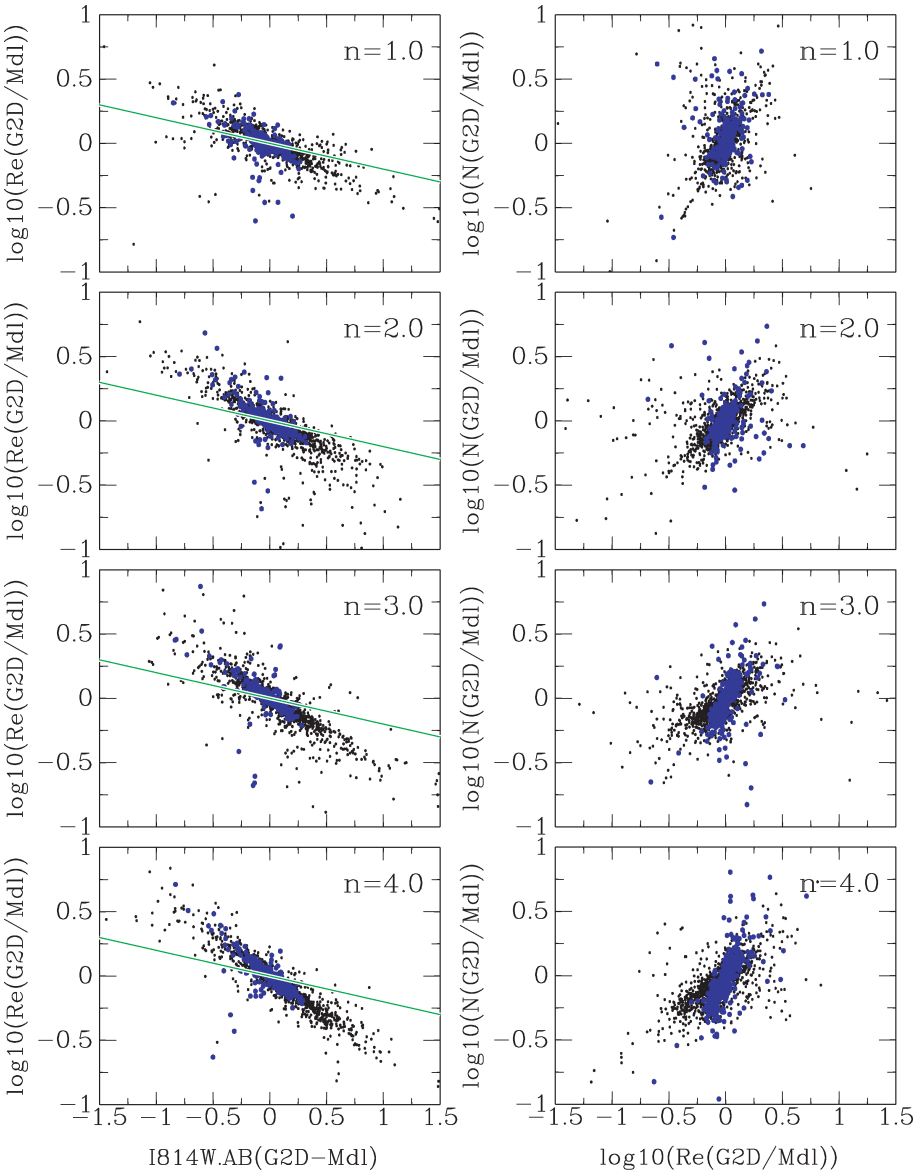

Figure 3. Effective radius residuals versus magnitude residuals (left-hand panels) and Sérsic index residuals versus effective radius residuals (right-hand panels) as a function of the input Sérsic index and $\langle\mu\rangle_e$. The residuals are defined as the ratio of the output value from GIM2D to the input model value. From top to bottom, the panels include sources with input Sérsic index $0.5 < n < 1.5$, $1.5 < n < 2.5$, $2.5 < n < 3.5$, and $3.5 < n < 8.0$, respectively. The larger blue dots represent points with input $\langle\mu\rangle_e$ brighter than 22.0, and the small black dots represent the whole pool of models created. The diagonal green line shows the location of the points should the fitting process preserve the mean effective surface brightnesses of the models. Deviations from this line indicate that GIM2D was not able to accurately retrieve the value of $\langle\mu\rangle_e$. Also, the slope of the clouds is correlated with the intrinsic profile of the model being fit. For galaxies with large n, it is somewhat more difficult to reproduce the parameters of the input model. The right set of panels shows how the fits to the models expand or compress, depending on whether the fit overestimates or underestimates R_e.

between 2.0 and 60.0 pixels. Sérsic indices were randomly distributed between 0.5 and 4.5. Ellipticities were randomly distributed from 0.0 to 0.8 and position angles were unconstrained. Of the total number of model galaxies created, 10 000 were both detected by SExtractor and successfully analysed by GIM2D; the analysis presented in this subsection deals with these 10 000 fake sources. The remaining sources were either not detected by SExtractor or fell in problematic areas of the image such as the CCD edges and were thus rejected.

The first step in the analysis of these simulations is presented in Fig. 3. This figure shows the magnitude residuals against the effective radius residuals, and the effective radius residuals against the Sérsic index residuals. These relations are presented in different panels, according to the input n as indicated in the figure. The points with an input $\langle\mu\rangle_e$ brighter than 22.0 are highlighted in blue.

As expected, the residuals in total magnitude anti-correlate with those in effective radius: where GIM2D yields a higher than expected luminosity, it also yields a higher than expected effective radius. This occurs for all Sérsic indices. The oblique, green line shows the error correlation that would preserve the mean effective surface brightness within one effective radius. The figure shows that GIM2D introduces a surface brightness bias: overluminous solutions have fainter $\langle\mu\rangle_e$. The slope of this covariance is found to be Sérsic index-dependent. The contraction or expansion of the fitted functions

with respect to the input parameters is not arbitrary, it depends on the real profile of the underlying source being fitted. Although these observations merely confirm an expected behaviour given the experiment being run, they are important because they allow us to use these simulations to assess the errors on the output parameters.

Comparable behaviour can be seen in the right-hand panels of Fig. 3. If GIM2D finds R_e higher than the real value, the output n is also higher than the real value. This happens because n is essentially determined by the pixels in the object wings, which are much more abundant and have higher weighting due to the lower Poisson noise, thus GIM2D has to increase the model power in these wings.

In addition, the fact that the Sérsic index has such a large impact on the behaviour of the residuals implies that this parameter has to be included in our recipe for error assessment (see also Marleau & Simard 1998, their fig. 11).

Fig. 4 shows the magnitude, effective radius and Sérsic index residuals against both input and output mean effective surface brightness for the 10 000 simulations. This figure is divided into four panels: for Sérsic indices of $0.5 < n < 1.5$, $1.5 < n < 2.5$, $2.5 < n < 3.5$ and $3.5 < n < 8.0$, respectively. The black lines with error bars give the run of the median value of the residuals and a robust estimate of the vertical 1σ scatter of the residuals around this latter median value. These median values of the residuals and their associated 1σ scatter have been calculated in equally spaced bins in *input* (left-hand panels) and *output* (right-hand panels) mean effective surface brightness. For clarity, the vertical 1σ scatter values are plotted separately in Fig. 5.

From the data presented in Figs 4 and 5, we find that, for $\langle\mu\rangle_e \leqslant 24.0$, the median values of $\Delta\log(n)$, $\Delta\log(R_e)$ and Δmag (the systematic errors) are always less than 0.05, 0.04 and 0.08, respectively. These values are only weakly dependent upon n, with the highest Sérsic index bin having smaller systematic errors (less than 0.05, 0.03 and 0.05, respectively). For brighter surface brightness ($\langle\mu\rangle_e \leqslant 21.0$), these differences are lower than 0.02, 0.03 and 0.04. The widths of the distributions, which we associate with the non-systematic error in the recovery of the input values, increase towards lower surface brightness and are, at the faintest limit, 0.12 dex, 0.15 dex and 0.25 mag, for $\log(n)$, $\log(R_e)$ and total magnitude, respectively. These values and figures indicate that, with the use of the tailored masks, GIM2D is indeed able to recover the input parameters accurately. The use of these customized masks and the use of the individualized search in the parameter space allows GIM2D to have a better understanding of the galaxy flux and size. This naturally leads to a better fit, free from the systematic errors that were detected by Häussler et al. (2007) and confirmed in Appendix A.

Figs 4 and 5 indicate that it is reasonable to use the output Sérsic index and $\langle\mu\rangle_e$ to derive realistic error estimates to the total magnitudes, effective radii and Sérsic indices. Given the modest number of simulations, we adopt a simple two-parameter approach based upon the output $\langle\mu\rangle_e$ and n. A single straight line of the form:

$$\log\sigma = \alpha \times \langle\mu\rangle_{e,out} + \beta, \quad (5)$$

is fit to the robust 1σ vertical scatter around the median shown in the right-hand panels of each quadrant of Fig. 5. Although this functional form is expected for the magnitude uncertainties, it is also used for the uncertainties in R_e and Sérsic index for simplicity. Table 1 shows the best-fitting coefficients for these fits.

To assign meaningful and realistic statistical errors to any GIM2D measurement, we first calculate the output $\langle\mu\rangle_e$. Next we evaluate the linear functional form given above using the coefficients found in Table 1. The final uncertainty in the parameter of interest, as given in the structural catalogue, is the anti-logarithm of the result.

Finally, the run of the errors with $\langle\mu\rangle_e$ and n, given in Fig. 5 and derived from the coefficients in Table 1, allow us to infer a limiting output $\langle\mu\rangle_e$ beyond which GIM2D will not be able to successfully recover the true parameters. We choose an operational limit of an uncertainty of 0.25 mag. This limit corresponds to S/N <5.0, and given the coefficients in the table, the corresponding limiting $\langle\mu\rangle_e$ is 24.5 mag arcsec^{-2}. Since the magnitude is the first moment of the light distribution of any object, it will not be possible to reliably recover the remaining structural parameters, which would be higher moments, from lower surface brightness objects.

4 GALFIT FITTING

This section describes the GALFIT (version 2.0.3c) set-up used to fit the program galaxies as well as the simulations carried out for error assessment. Nearly all galaxies included in the SExtractor catalogue presented in Paper II were fit, except for the sources that were originally buried in the extended haloes of large galaxies. GALFIT is capable of fitting multiple galaxies simultaneously. Because its χ^2 minimization algorithm is based on a gradient method, it is significantly faster than GIM2D. However the algorithm is susceptible to getting stuck in a local minimum. For the fit to converge quickly to the correct values, it is essential that the initial values of the parameters are as close to the real solution as possible.

Most initial parameters that we use for fitting are based on the SExtractor catalogue. When fitting large numbers of galaxies, any manual intervention is extremely time consuming. Therefore, we decided to make use of ASTRO-WISE,[2] which provides a facility for the structural analysis of large data sets.

4.1 GALFIT set-up in ASTRO-WISE

ASTRO-WISE is an information system and environment for large imaging data sets, up to the petabyte regime, with multiple users around Europe. In ASTRO-WISE one can archive raw data, calibrate data and perform scientific analysis storing all results. Valentijn et al. (2007) provide a technical description of the information system, and Sikkema (2009) describes the data reduction pipeline.

The scientific analysis components in ASTRO-WISE include, among others, routines for source extraction (using SExtractor), variability analysis, photometric redshifts and galaxy surface photometry fitting using GALFIT. The GALFIT implementation within ASTRO-WISE automatically produces the specified postage stamps of the sources, runs GALFIT itself and stores the configuration and results for all sources in a data base. ASTRO-WISE enables full backward-chaining of data lineage in general. This means that model image, residual image and customized inspection plots can be created anytime upon request.

We use the GALFIT set-up of Häussler et al. (2007) as a starting point for our fitting scheme. Here we present a detailed description of the fitting process.

First, ASTRO-WISE makes a postage stamp of each source. The size chosen is slightly larger than that of Häussler et al., and is determined from the SExtractor image size measurements, such that

$$\text{size} = 4 \times \text{A\_IMAGE} \times \text{KRON\_RADIUS}. \quad (6)$$

[2] www.astro-wise.org

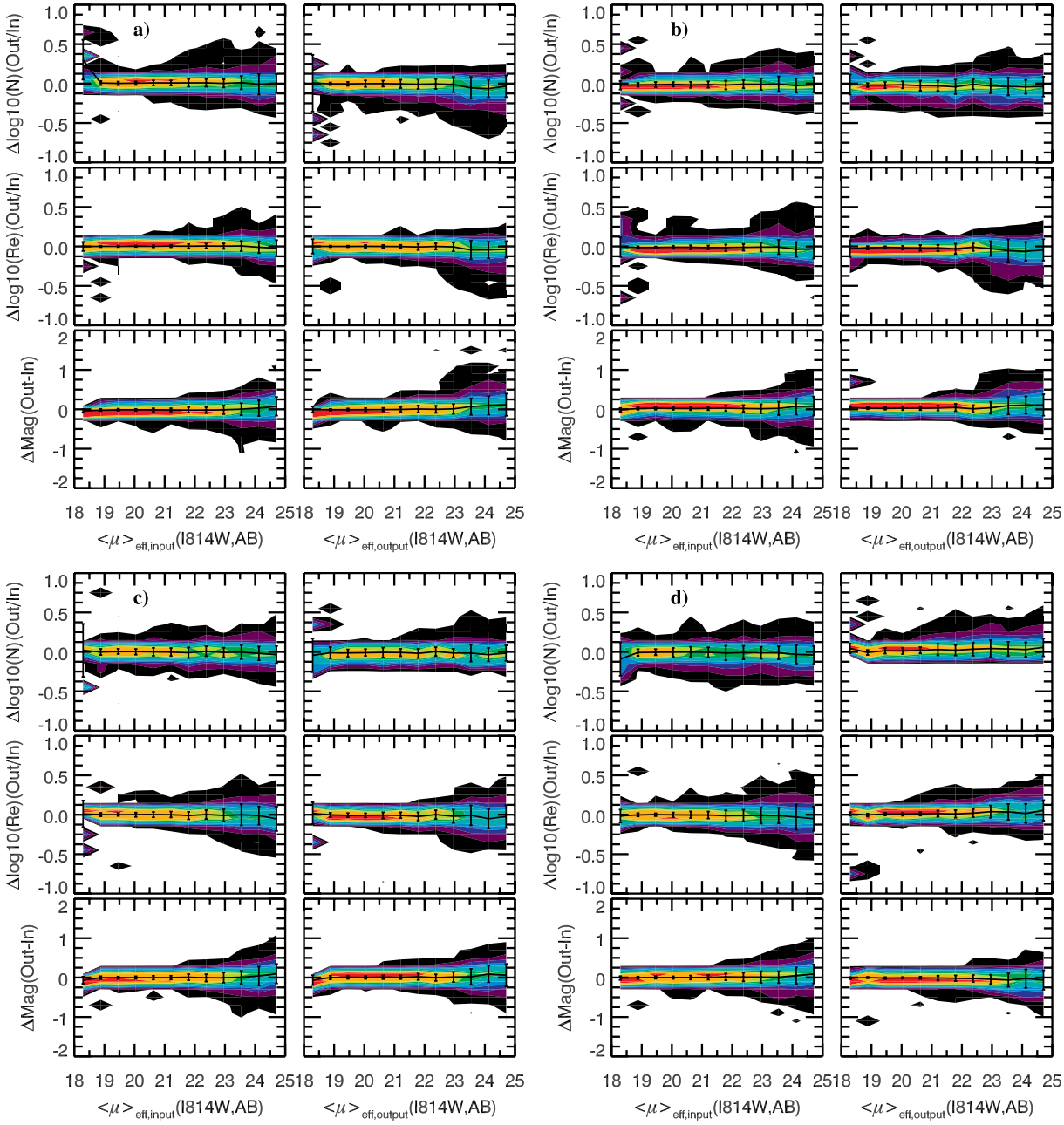

Figure 4. Magnitude, effective radius and Sérsic index residuals for the GIM2D simulations. This figure is divided into four quadrants, each with six panels. Top left quadrant (a) shows the residuals for simulations of galaxies with input $0.5 < n < 1.5$; top right quadrant (b) simulations with input $1.5 < n < 2.5$, bottom left quadrant (c) simulations with input $2.5 < n < 3.5$ and bottom right quadrant (d) simulations with input $3.5 < n < 8$. In each quadrant, the top two panels show the residuals in Sérsic index as a function of input $\langle\mu\rangle_e$ (left) and output $\langle\mu\rangle_e$ (right) panels. The middle two panels show the residuals in R_e and the bottom two the residuals in magnitude, again against input and output $\langle\mu\rangle_e$. The lines with vertical error bars show the run of the median value of the residuals; the error bars are 1.5 times the interquartile width of the vertical distribution. The colour coding shows the two-dimensional histogram of the density of the underlying points, normalized along the vertical axis only. The lowest level (black) has a density >1 per cent of the maximum, and the highest level (red) is >50 per cent of the maximum. Intermediate shades are at 5, 10, 15, 20, 30 and 40 per cent.

Next, a sigma image is created from the inverse variance map. This sigma image is modified to take into account Poisson noise from the sources as well.

Nearby sources are masked according to the SEXTRACTOR segmentation image. In line with the GEMS results and encouraged by the results with GIM2D, we expand the masks for nearby sources by using elliptical apertures with semimajor axis 4 × 1A_IMAGE1 and with ellipticity and position angle as determined by SEXTRACTOR. Sources for which this mask overlaps with the mask of the main source are fitted by GALFIT together with the main source.

The implementation of the Sérsic profile in GALFIT has eight free parameters. Of these, we leave the disciness/boxiness parameter fixed so that all isophotes describe perfect ellipses. All other parameters are left free. In addition to this, we leave the

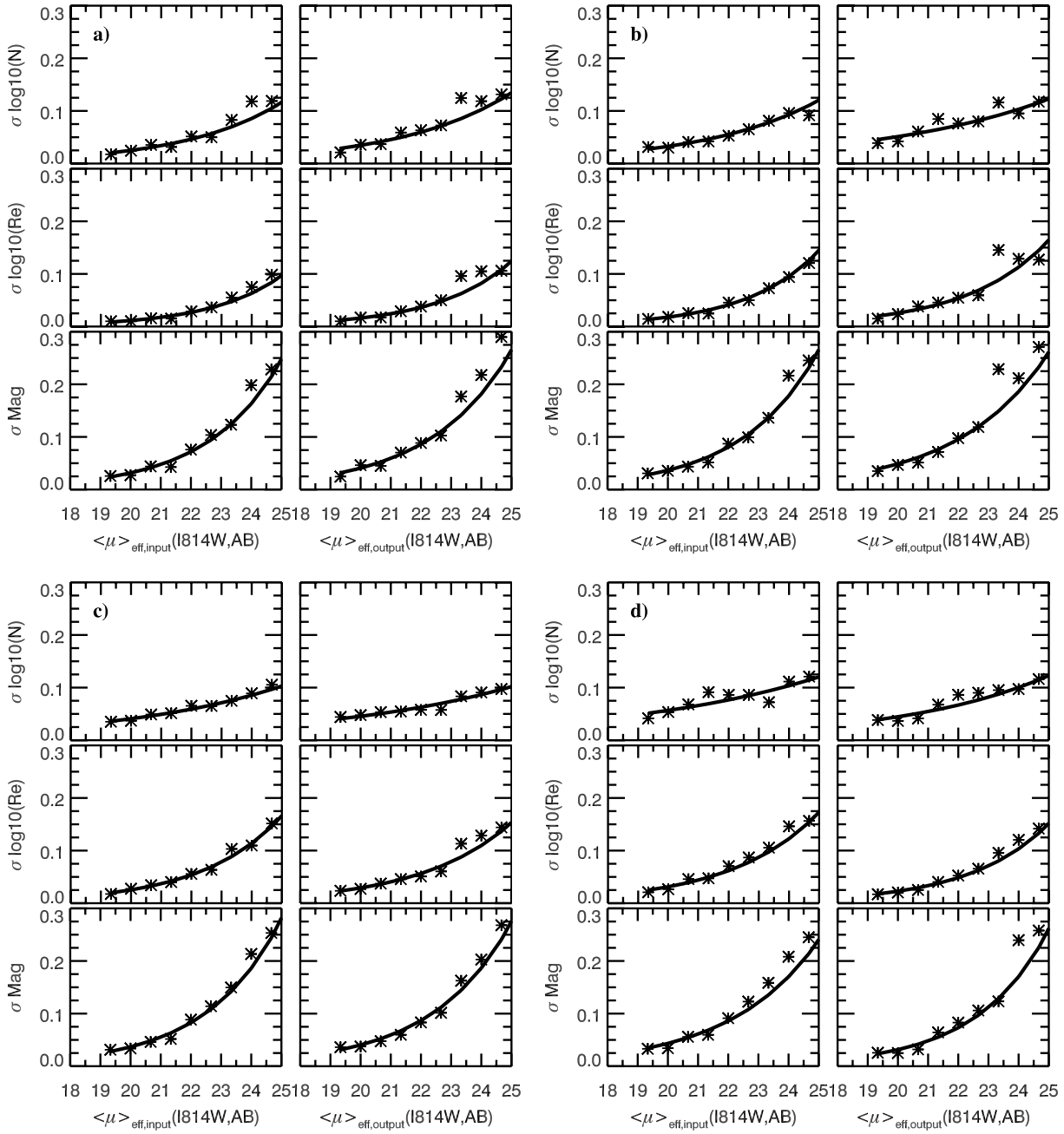

Figure 5. Amplitude of the error bars for the GIM2D simulations plotted in Fig. 4. The figure layout is identical to that of Fig. 4. In each panel, the right-hand panels provide a direct measure of the $\langle\mu\rangle_e$ dependence of the non-systematic error in each of the model parameters $\Delta\log(n)$, $\Delta\log(R_e)$ and Δmag.

sky free, although we do not allow for any gradient in the sky. We do, however, constrain n to the interval [0.5, 8.0]. Gradient based fitting methods do require an initial guess for all parameters. Except for the Sérsic index, which we initialize as $n = 1.5$ for all sources, initial guesses for each source are based on parameters from the SEXTRACTOR catalogue: for R_e we use FLUX_RADIUS[3], for total magnitude we use MAG_ISO. The axial ratio and position angle are initialized from ELLIPTICITY and THETA_IMAGE.

ASTRO-WISE uses these parameters to write a configuration file for GALFIT. In the case of multi-object fitting, we determine the input parameters for the secondary objects in the same way, with the exception that we keep the position of the source fixed if its centre is outside the postage stamp.

4.2 Shot-noise simulations

Similarly to what was done for GIM2D (Section 3.4), an extended set of simulations were performed. The simulations serve three main purposes. First, they allow us to test our GALFIT set-up, by identifying biases in the fits. Secondly, they allow us to infer realistic errors of the output parameters. Like GIM2D and other fitting codes,

Table 1. Table of coefficients required to use equation (5) to estimate the statistical errors on the total magnitude, R_e and n, for various ranges of output n, for the GIM2D fits.

Magnitude	Sérsic index	β	α
	$0.5 < n < 1.5$	−4.64	0.16
	$1.5 < n < 2.5$	−4.22	0.15
	$2.5 < n < 3.5$	−4.72	0.17
	$3.5 < n < 8.0$	−5.17	0.18
$\log R_e$(G2D/Model)	Sérsic index	β	α
	$0.5 < n < 1.5$	−5.34	0.18
	$1.5 < n < 2.5$	−4.83	0.16
	$2.5 < n < 3.5$	−4.43	0.14
	$3.5 < n < 8.0$	−4.93	0.16
$\log n$(G2D/Model)	Sérsic index	β	α
	$0.5 < n < 1.5$	−3.81	0.12
	$1.5 < n < 2.5$	−2.81	0.08
	$2.5 < n < 3.5$	−2.74	0.07
	$3.5 < n < 8.0$	−3.11	0.09

Table 2. Input simulation parameters of GALFIT single Sersíc galaxies. All quantities are cast uniformly in the given range, except R_e and n, which are cast uniformly in logarithmic space. The number of bins denotes into how many bins the range was divided for the final error assessment. In the GALFIT simulations, the effective surface brightness rather than the mean effective surface brightness was used to define the bins.

Parameter	Range	#Bins
x (pix)	400.0–4000.0	–
y (pix)	400.0–4000.0	–
Mag	20.0–25.0	6
R_e	2.0–60.0 (log)	10
n	0.5–6.0 (log)	5
μ_e	<25.5	–
Ell	0–0.8	2
Pos	0.0–180.0	–

GALFIT tends to underestimate errors on the fitted parameters (cf. Häussler et al. 2007). Our simulations allow us to assign errors to fitted parameters which are more realistic than the standard GALFIT errors. (Our errors are still lower limits because images of real galaxies deviate from the perfect Sérsic model with concentric, coaxial isophotes.) Finally, the simulations allow us to define limits for the minimum S/N required for reasonable fits. The simulations were not designed to test the performance of GALFIT in crowded areas, which has already been extensively discussed by Häussler et al. (2007).

GALFIT is wrapped in ASTRO-WISE using the PYTHON language which allows for straightforward customization and script writing for a specific science case. We adapted the PYTHON code in ASTRO-WISE to create simulated galaxies, insert them into images, create source lists and then to run GALFIT on them. As is the case with GIM2D, GALFIT's ability to correctly fit a given galaxy varies with the intrinsic parameters of the fitted galaxy. Hence, to assign errors to the fit parameters of real galaxies, we require the results of a large number of simulated galaxies with similar output parameters.

In our approach we created a mock catalogue of 200 000 galaxies. The parameter ranges used are listed in Table 2. Each parameter samples the given range, either uniformly or uniformly in the log as indicated in the table. The parameter ranges were chosen so that the distributions of output parameters bracket the distributions found in the data. When generating these parameters, we avoided the edges of the frame and applied a hard cut-off in μ_e to avoid any detection problems with SEXTRACTOR.

After each model galaxy had been fitted by GALFIT, the distributions of the differences output *minus* input were binned in order to determine the variation of the errors with key *output* parameters such as magnitude, surface brightness and Sérsic index. We chose six bins in magnitude, 10 bins in $\log(R_e)$, two bins in ellipticity and five bins in n (600 bins in total). To minimize the uncertainty on the errors, one would like to have as many galaxies per bin as possible. Our 200 000 models yield $\sim$330 bin^{-1}, so that, even though for some galaxies the output bin will be different from the input bin and certain output bins will be more sparsely populated than others, the relative uncertainty on the errors (assuming they are Gaussian) is always less than 10 per cent.

GALFIT itself was used to generate the artificial galaxy models. Although one might argue that using GALFIT to make the two-dimensional images to which itself it should fit models is doubtful, we stress that GALFIT has been tested extensively and that, in our opinion, it is doing at least a better job than IRAF.ARTDATA, which does not sufficiently oversample in the centres of galaxies. Our simulation set-up takes into account convolution of the model galaxies with a DRIZZLYTIM PSF. Before injecting them into real ACS observations, Poisson noise was added to these galaxies. To avoid any crowding, we used only 100 models per ACS frame, so that we ended up with 2000 frames, each with 100 artificial galaxies on top of the $\sim$2500 sources already present. Simulated galaxies were injected into visit 90, because this frame is relatively empty and on does not suffer from any missing dithers.

On each frame with simulated galaxies, we ran SEXTRACTOR using the same configuration as was used for the real data (see Paper II). We associated our list of simulated sources with the sources detected by SEXTRACTOR by demanding that they be at most 14 pixels away from the closest source in the catalogue. A small fraction ($\sim$1 per cent) of sources were not detected by SEXTRACTOR. In a small number of cases, SEXTRACTOR can be confused by proximity to or even blending with a source already present in the frame.

Results of the simulations are shown in Figs 6 and 7. As in Fig. 4, Fig. 6 shows residuals of the logarithm of the Sérsic index $\log(n)$, the logarithm of the effective radius $\log(R_e)$ and the total magnitude, against input (left) and output (right) mean effective surface brightness $\langle\mu\rangle_e$. In general, the distributions of the output parameters around the mean have non-Gaussian, extended wings. Hence, a standard rms error does not allow for a straightforward interpretation. Rather than determining the rms of a outlier-clipped sample, we use a 95 per cent confidence interval determined from the interquartile range per surface brightness or magnitude bin. The symmetrized intervals are used as error bars in the plots in Fig. 6, and plotted again in Fig. 7.

The results are excellent and, overall, similar to those obtained with GIM2D (Section 3.4). Up to $\langle\mu\rangle_e = 24.0$, the median differences, or systematic errors, are below 0.04 dex, 0.02 dex and 0.04 mag, in $\log(n)$, $\log(R_e)$ and total magnitude, respectively, except for the highest Sérsic index bin where the differences at $\langle\mu\rangle_e = 24$, are always lower than 0.06 dex, 0.06 dex or 0.07 mag. The slight bias pattern that appears for $\langle\mu\rangle_e > 24.0$ and high Sérsic indices, (Fig. 6c,d), is an boundary effect of the simulation set-up. Output models are brighter, and have larger R_e, than the input values due to the fact that input models only reach $\langle\mu\rangle_e \lesssim 24.0$. The region with output $\langle\mu\rangle_e > 24.0$ is only populated with models for which GALFIT

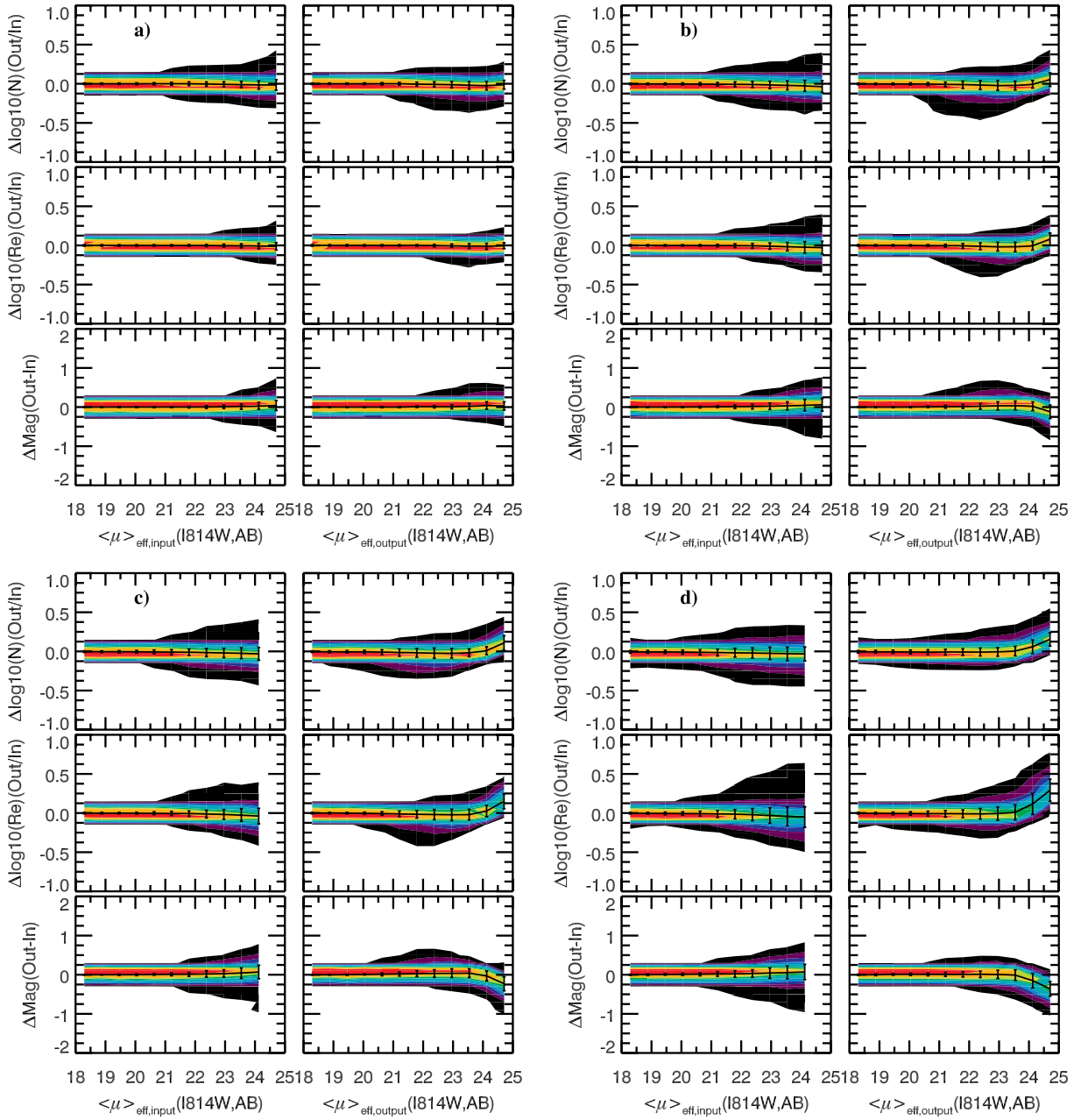

Figure 6. Magnitude, effective radius and Sérsic index residuals for the GALFIT simulations. This figure is organized as Fig. 4. Magnitude, effective radius and Sérsic index residuals for the GIM2D simulations. This figure is divided into four quadrants, each with six panels. Top left quadrant (a) shows the residuals for simulations of galaxies with input $0.5 < n < 1.5$; top right quadrant (b) simulations with input $1.5 < n < 2.5$, bottom left quadrant (c) simulations with input $2.5 < n < 3.5$ and bottom right quadrant (d) simulations with input $3.5 < n < 6$. In each quadrant, the top two panels show the residuals in Sérsic index as a function of input $\langle\mu\rangle_e$ (left-hand) and output $\langle\mu\rangle_e$ (right-hand) panels. The middle two panels show the residuals in R_e and the bottom two the residuals in magnitude, again against input and output $\langle\mu\rangle_e$. The lines with vertical error bars show the run of the median value of the residuals. As in Fig. 4, the error bars are given by 1.5 times the interquartile range. The colour coding shows the two-dimensional histogram of the density of the underlying points, normalized along the vertical axis only. The lowest level (black) has a density >1 per cent of the maximum, and the highest level (red) is >50 per cent of the maximum. Intermediate shades are at 5, 10, 15, 20, 30 and 40 per cent.

has found a solution with fainter $\langle\mu\rangle_e$. Because the errors in R_e and $\langle\mu\rangle_e$ are coupled, these models must have positive R_e residuals (as observed in the middle-right panels of Fig. 6c,d).

The run of non-systematic errors with input and output mean effective surface brightness (Fig. 7) shows similar behaviour to those of the GIM2D errors (Fig. 5). For a given surface brightness, GALFIT errors tend to be slightly smaller than GIM2D errors but the differences are not meaningful, given that GIM2D values are more uncertain owing to the lower number of GIM2D simulations.

In Table 3, we present the parameters needed to estimate the uncertainties of the GALFIT output parameters, as was previously done in Table 1 for GIM2D. This gives the coefficients for the fits of

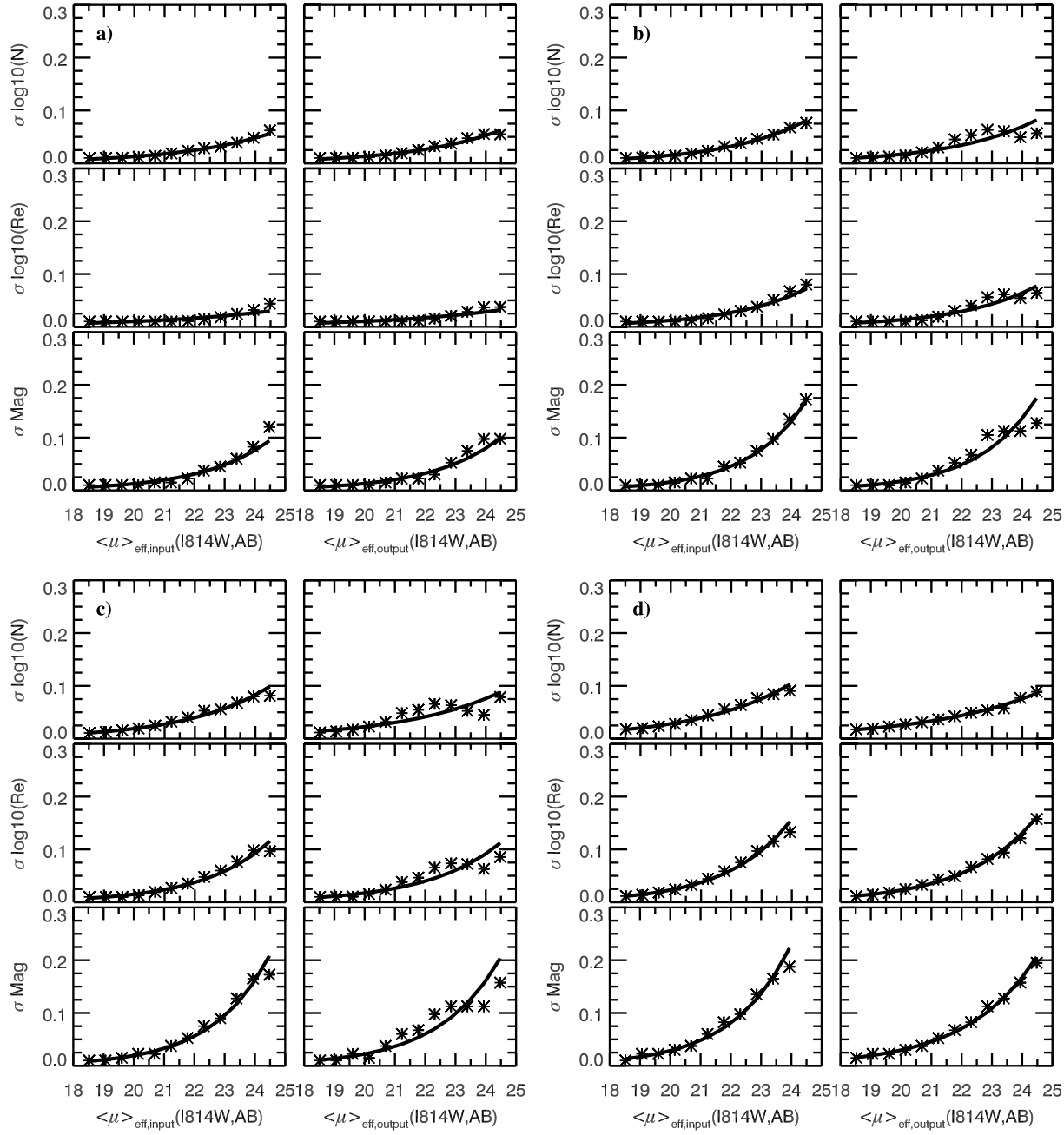

Figure 7. Amplitude of the error bars for the GALFIT simulations plotted in Fig. 6. The figure layout is identical to that of Fig. 6. In each panel, the right-hand panels provide a direct measure of the $\langle\mu\rangle_e$ dependence of the non-systematic error in each of the model parameters $\Delta\log(n)$, $\Delta\log(R_e)$ and Δmag.

equation (5). The best-fitting relations were then applied to extract the error estimates for each of the Sérsic parameters that are given in the published structural catalogue.

The simulations were also used to provide a reasonable faint limit in surface brightness that gives realistic results. A conservative approach was used to define this limit, which we also set to be the same as that applied for the GIM2D fits.

4.3 Small-size limit of GALFIT

With the discovery of 16 new ultra compact dwarfs in the Coma cluster (Chiboucas et al. 2010b) it is important to quantify how small an effective radius we can measure. To see how well GALFIT can recover radii and magnitudes for small sources, 20 000 further simulations were carried out. The parameter space covered by this new set of simulations is presented in Table 4.

We find from this new set of simulations that the recovered effective radii are unbiased, however for very small sources (R_e < 0.5 pixels) GALFIT sometimes falls back to a hard-coded lower limit of $R_e = 0.01$ pixel. This means that even for the perfect conditions assumed in the simulations, the number of recovered sources that have R_e around 0.5 pixel will be fairly incomplete. It is very difficult for GALFIT to differentiate between a genuine point source and a small, yet extended, $R_e < 0.5$ pixel source. These

Table 3. Table of coefficients required to use equation (5) to estimate the statistical errors on the total magnitude, R_e and n, for various ranges of output n, for the GALFIT fits.

Magnitude	Sérsic index	β	α
	$0.5 < n < 1.5$	−1.70	0.036
	$1.5 < n < 2.5$	−1.30	0.020
	$2.5 < n < 3.5$	−1.65	0.035
	$3.5 < n < 8.0$	−2.62	0.079
$\log R_e$(GF/Model)	Sérsic index	β	α
	$0.5 < n < 1.5$	−3.90	0.12
	$1.5 < n < 2.5$	−3.57	0.11
	$2.5 < n < 3.5$	−4.42	0.15
	$3.5 < n < 8.0$	−3.58	0.11
$\log n$(GF/Model)	Sérsic index	β	α
	$0.5 < n < 1.5$	−4.09	0.13
	$1.5 < n < 2.5$	−3.17	0.092
	$2.5 < n < 3.5$	−3.01	0.084
	$3.5 < n < 8.0$	−2.77	0.075

Table 4. Parameters of simulated galaxies for the small radii simulations. Same comments as for Table 2 apply. $R_{\rm eff}$ and n are logarithmically spaced. As with Table 2, the limit in surface brightness is defined in terms of μ_e not $\langle\mu\rangle_e$.

Parameter	Range	Remark
x	400.0–4000.0	
y	400.0–4000.0	
Mag	22.0–26.5	
R_e	0.1–5.0	Log
n	0.5–6.0	Log
μ_e	<25.5	
Ell	0–0.8	
Pos	0.0–180.0	

simulations assume perfect knowledge about the PSF, and model only the background contribution to the noise. Furthermore, the sources were injected on a relatively empty frame (visit 90). To see how well GALFIT performs on real point sources, we inspect the effective radii of sources in visit 19, the visit which covers the galaxy NGC 4874. A large number of the sources in this visit are thought to be globular clusters (Peng et al. 2010), which should be unresolved at the distance of 100 Mpc. Fig. 8 shows a histogram of *measured* effective radii for this visit. It looks as if the distribution of sources is shown by a power law, plus an additional group of sources distributed around $R_e \sim 0.5$ pixel, with a standard deviation ∼0.3 pixel. We conclude that GALFIT output giving $R_e \sim 0.5$ pixel is likely to come from point sources. From the shape of the blue histogram in Fig. 8, we infer that $R_e > 1$ pixel provides a robust lower limit for GALFIT R_e's.

5 GOODNESS-OF-FIT INDICES

Although the Sérsic model is a well known and tested fitting function, real galaxies are more complicated. They present, among many other features, stellar bulges, star forming regions, active galactic nuclei, spiral arms, extended haloes and central star clusters.

In this section we define two complementary diagnostic indices, each designed to address in a different way the question of whether the Sérsic model is an adequate fit, given the available data, or whether a more complicated function or extra components are required. These diagnostics are calculated for all fits.

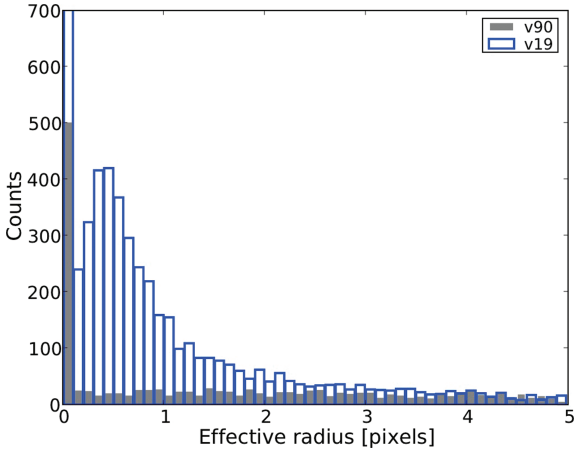

Figure 8. Histogram of GALFIT Measurements of the R_e for the sources found in visits 19 and 90. The filled histogram represents the sources in visit 90, i.e. a field with few Coma galaxies. The open histogram is the histogram of visit 19, with many Coma galaxies and globular clusters.

Following Blakeslee et al. (2006), we define the residual flux fraction (RFF) as

$$\mathrm{RFF} = \frac{\left(\sum_i |\mathrm{Res}_i| - 0.8\sigma_{\mathrm{image}}\right)}{\mathrm{FLUX\_ISO}}, \quad (7)$$

where the summation is over all pixels within the ISOAREA of that particular object, $|\mathrm{Res}_i|$ is the absolute value of residual image obtained by subtracting the best-fitting model from the real galaxy image, and FLUX_ISO is the total flux within the ISOAREA, which can be taken from SEXTRACTOR.

This index measures that part of the sum of the modulus of the pixels in the residual image which cannot be explained by the experimental error. The image variance is obtained from the usual CCD equation as

$$\sigma^2_{\mathrm{image}} = \sigma^2_{\mathrm{bkg}} + \frac{S}{g}, \quad (8)$$

where S is the value of the model for that pixel and g is the effective gain, which can be found from the SEXTRACTOR parameters for the particular image.

RFF quantifies the residual signal which cannot be explained by arguing that the fitting codes found a suboptimal minimum. It is best understood as a hypothesis testing procedure.

If the real galaxy had a pure Sérsic profile, both GIM2D and GALFIT could find a model providing an exact fit to the galaxy. However, even in this optimal case, the errors associated with the readout noise and photon shot noise imply that the residual image will not be blank. In the case of independent errors, the properties of the residual image would be very similar to those of Gaussian white noise, with a spatially varying σ. The expectation value of the sum of the absolute values of these residuals is $\sum 0.8 \times \sigma_{\mathrm{image}}$. Therefore, the expectation value of the numerator of the RFF is 0.0, *should galaxies be pure Sérsic models*. Since the denominator is a normalization factor, the expected value of the RFF itself is 0.0 for such a model. Any positive or negative deviation from a pure Sérsic model will increase the RFF. From our own visual experience with this index, we find that fits with an RFF larger than 0.11 indicate that a more complex fit is required. This number was agreed after independent experiments made by CH and RG.

The RFF diagnostic does not work well for objects with large ISOAREAS, and low $\langle\mu\rangle_e$. In these cases, as both the galaxy and the model decay towards zero at large radii, the outer areas will dominate the RFF calculation, and even though the fit may have complicated and highly non-Gaussian residuals at small radii, RFF will still be small.

Hence we require a second diagnostic, which should be particularly sensitive to the central residuals. This is calculated from the same set of pixels within the isophotal area of the target galaxies as RFF.

This complementary parameter is the excess variance index (EVI). It is defined as

$$\mathrm{EVI} = \frac{1}{3} \times \left(\frac{\sigma_R^2}{\langle \sigma_{\mathrm{image}}^2 \rangle} - 1 \right), \quad (9)$$

where σ_R is the root mean square of the residuals within the ISOAREA, and $\langle\sigma^2_{\mathrm{image}}\rangle$ is the mean value of the square of the noise within the same area. EVI gives a measure of the granularity excess of the actual residuals with respect to the expected granularity.

For pure Sérsic models, the numerator in the EVI expression above would simply be a sum of squares of normally distributed random variables with zero mean and pixel-dependent variance. The expectation value of the numerator would be, in this case, the value of the denominator. Hence, the parenthesized expression in the EVI definition has an expectation value of 0.0, and strong deviations from 0.0 indicate that the underlying real galaxy differs significantly from a Sérsic model. Given the EVI definition, such deviations would most likely be caused by the points with the largest intrinsic standard deviations (i.e. the inner points). This makes this index particularly sensitive to the structure of the residuals at small radii. The 1/3 factor in the definition of the EVI was later added so that residual images with an EVI larger than approximately 1.0 present complicated substructure in the inner parts of the fits, whilst objects with an EVI smaller than approximately 1.0 show acceptable fits. In the end, after several iterations of this by eye calibration carried out by CH and RG, it was concluded that residuals with an EVI larger than 0.95 indicate complex residuals.

5.1 Comparison of the diagnostic indices

Since the RFF and EVI indices were designed to see whether a single Sérsic fit is sufficient, it is reasonable to ask how well the GIM2D and GALFIT agree on this issue. As a first check, we plot in Fig. 9 the RFF and EVI indices of GALFIT against their GIM2D counterparts. There is a strong correlation between the indices for the two codes. However, there is also a small offset present, in the sense that the GIM2D indices are on average slightly higher than the GALFIT indices. We attribute this to a different treatment of the noise in the calculation of the two indices (the GALFIT indices were calculated using the sky noise from the IVM maps, whereas for the GIM2D indices we used the noise as estimated by GIM2D itself.) For high values of RFF and EVI the correlation breaks down. Especially for EVI, there are galaxies where the GIM2D index is normal, but the GALFIT index is larger. In part this is the result of fitting low S/N sources, where GALFIT has a preference for fitting a low surface brightness model to fluctuations in the background instead of fitting the source itself.

In Fig. 10, we show histograms of the RFF for different magnitude bins. If all sources were perfect Sérsic galaxies, these should take the form of a Gaussian, where the width is dependent on the S/N. We find many faint sources with RFF < 0. We interpret this as overfitting: RFF < 0 means that there is less noise in the image than expected, so the code has modelled the noise away. For larger

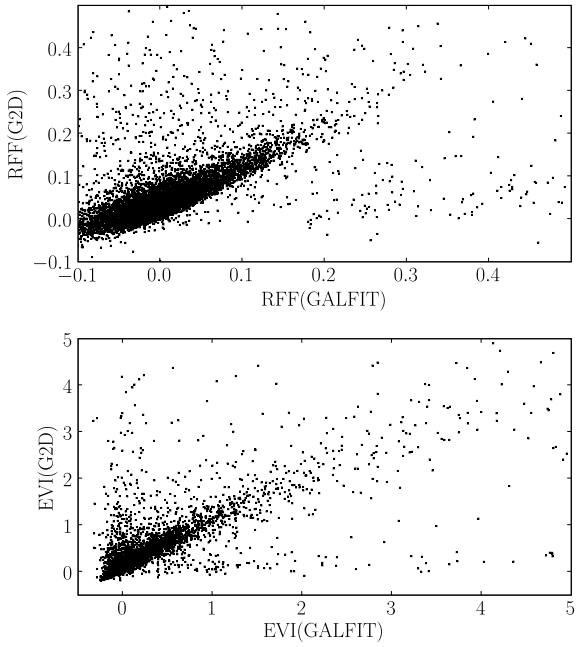

Figure 9. Top panel: RFF from GALFIT plotted against that from GIM2D; lower panel: EVI from GALFIT plotted against that from GIM2D.

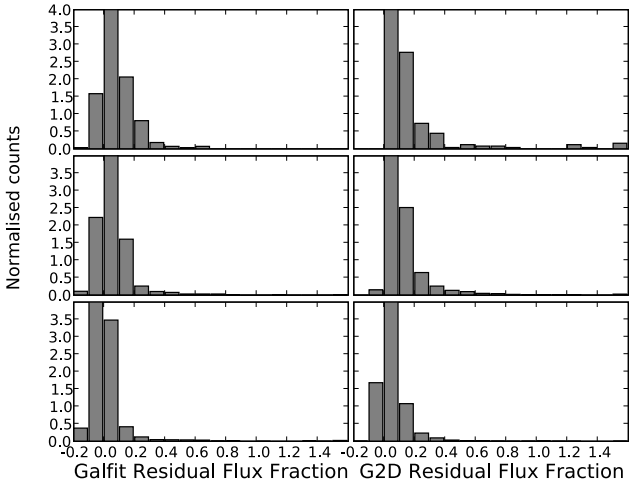

Figure 10. The RFF calculated for our magnitude, size and surface brightness clipped sample on the residual images of both codes. The sample is divided in three magnitude bins: 17.5–19.0 in the upper panel, 19.0–22.0 in the middle panel and 22.0–25.0 in the lower panel.

galaxies this problem is of course less severe, as the code has to model more pixels with higher S/N, so it has less freedom.

Fig. 11 shows the calculated EVIs, for the same magnitude bins. Although the faint sources centre around zero, the brightest magnitude bins show a large fraction of high EVIs. It is only in the brightest galaxies that we can see the deviation from the Sérsic profile (top panels), because of the high S/N and spatial resolution. For the faint sources, the data are not good enough to detect any granularity.

These indicators will allow separation into subsamples of galaxies which are well represented by the Sérsic function, for studies of the scaling relations or for separation by morphological class, or of galaxies for which additional components, truncation or extension

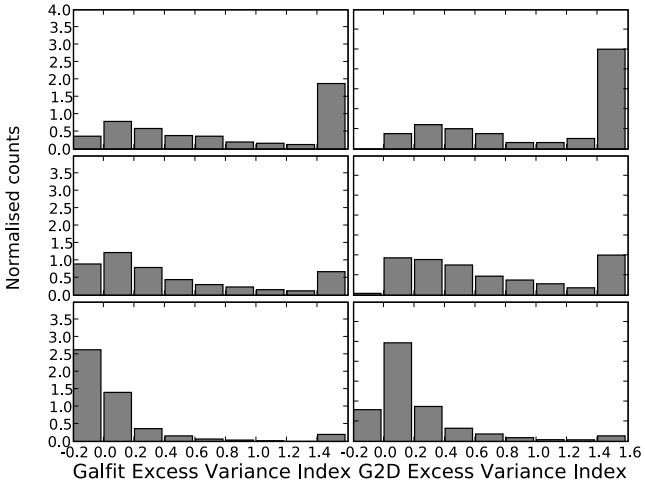

Figure 11. The EVI, see caption of Fig. 10 for more explanation.

of the light distributions show that they must be fitted with more complex functions.

6 THE CATALOGUE

This section introduces the main result of the present paper: the catalogue of structural parameters for the Coma-ACS survey based on single Sérsic fits. We provide a description of the catalogue and its limits in magnitude, radius and effective surface brightness.

The parameters presented in the final catalogue are summarized in Table 5, which presents the table headings of the released source lists together with a brief explanation of their meaning. In addition to best-fitting values for both GIM2D and GALFIT fitting, the catalogue includes coordinates and SEXTRACTOR photometry, and goodness-of-fit RFF and EVI for both codes.

Recalling that all 74 992 galaxies from the SEXTRACTOR photometric catalogue from Paper II were fitted with GIM2D and GALFIT, the full structural catalogue presented here contains all galaxies from the complete photometric catalogue which fulfil the selection criteria described in Section 6.1. This amounts to 8814 sources. The full version of the structural parameter catalogue can be found in the electronic version of this paper, in the ASTRO-WISE website and the *HST* MAST archive.

6.1 Surface brightness, magnitude and size limits

Although the two codes were used to fit all the sources detected by SEXTRACTOR in the $F814W$ ACS images, not all of the resulting output parameters are meaningful, and we apply limits in radius, magnitude and surface brightness to the final table, explained below.

The Monte Carlo simulations presented in Sections 3.4 and 4.2 indicate that the uncertainty and reliability of the output parameters depend critically on the S/N of the fitted sources. This is in turn a function of magnitude and surface brightness. Based upon these simulations, we find that the derived parameters and their errors are reliable for all sources for which: $F814W < 24.5$, and $\langle\mu\rangle_e < 24.5$.

Most galaxies for which $F814W \geqslant 24.5$ are likely to be background galaxies, and in any case are beyond the magnitude limit of current spectroscopic surveys, so cluster membership cannot be verified, and their use in structural studies would be limited. At the distance of the Coma cluster, the apparent magnitude limit corresponds to $M_{F814W} = -10.5$, which is well within the absolute magnitude distribution of globular clusters.

Table 5. Output parameters included in the structural parameter catalogue.

Col.	Parameter	Meaning
1	COMA_ID	Name of source, as it appears in Paper II.
2	RA (J2000)	Right ascension of source.
3	Dec. (J2000)	Declination of source.
4	MAG_AUTO_CORR.	Automatic $F814W$ magnitude from SEXTRACTOR catalogue, corrected according to the prescription discussed in Paper II.
5	$F814W$ (GF)	$F814W$ apparent magnitude of GALFIT model. No k- or extinction correction applied.
6	σ_{F814W} (GF)	Error on $F814W$, as calculated from the simulations described in the text.
7	R_e (GF)	Effective radius, in pixels from GALFIT model.
8	σ_{R_e} (GF)	Error on R_e, as calculated from the simulations described in the text.
9	n (GF)	Sérsic index from GALFIT model.
10	σ_n (GF)	Error on n, as calculated from the simulations described in the text.
11	μ_e (GF).	Surface brightness at R_e calculated from the GALFIT model.
12	$\langle\mu\rangle_e$ (GF)	Mean surface brightness within R_e calculated from the GALFIT model.
13	Ellip. (GF)	Ellipticity of model $(1 - b/a)$ as given by GALFIT.
14	$\sigma_{\rm Ellip}$ (GF)	Formal error on ellipticity from GALFIT.
15	θ (GF)	Position angle of source as given by GALFIT.
16	σ_θ (GF)	Formal error on θ from GALFIT.
17	RFF(GF)	RFF diagnostic, defined in the text, derived from the residuals from the GALFIT model.
18	EVI (GF)	EVI, derived from the residuals from the GALFIT model.
19	$F814W$ (G2D)	$F814W$ apparent magnitude of GIM2D model. No k- or extinction correction applied.
20	σ_{F814W} (G2D)	Error on $F814W$, as calculated from the simulations described in the text.
21	R_e (G2D)	Effective radius, in pixels from GIM2D model.
22	σ_{R_e} (G2D)	Error on R_e, as calculated from the simulations described in the text.
23	n (G2D)	Sérsic index from GIM2D model.
24	σ_n (G2D)	Error on n, as calculated from the simulations described in the text.
25	μ_e (G2D)	Surface brightness at R_e in the GIM2D model.
26	$\langle\mu\rangle_e$ (G2D)	Mean surface brightness within R_e calculated from the GIM2D model.
27	Ellip. (G2D)	Ellipticity of model $(1 - b/a)$ as yielded by GIM2D.
28	$\sigma_{\rm Ellip}$ (G2D)	Formal error on ellipticity from GIM2D.
29	Pos. ang. (G2D)	Position angle of source as given by GIM2D.
30	σ_θ (G2D)	Formal error on θ from GIM2D.
31	RFF(G2D)	RFF diagnostic, defined in the text, derived from the residuals from the GIM2D model.
32	EVI (G2D)	EVI, derived from the residuals from the GIM2D model.

We do find, however, that a number of galaxies with comparatively high *central* surface brightness, large R_e, and in some cases with measured redshifts, fall below the surface brightness limit of $\langle\mu\rangle_e = 24.5$. For this reason, we also include in our catalogue galaxies with $26.0 > \langle\mu\rangle_e > 24.5$, but we caution that because our simulations largely did not cover the parameter space occupied by these galaxies, we have less confidence in the derived structural parameters and their errors. For these sources for which only the *central* regions are detected, both codes are naturally forced to extrapolate a substantial part of the total surface brightness profile. In these cases, the results critically depend on the different hypothesis (e.g. constant sky) with which the codes work, and thus the derived parameters are more uncertain.

In the final catalogue, we include only sources for which $F814W < 24.5$ as measured with *both* codes, provided that both codes had converged. If only one code converged then the magnitude from that code is used. For inclusion, sources have to satisfy the surface brightness criterion for either of the codes, not both.

Besides magnitude and surface brightness cuts, we impose an R_e lower limit with the aim to eliminate point sources from the catalogue, since for these the parameters of the Sérsic fit have no meaning. From the simulations described in Section 4.3, we have decided to reject sources for which either code measures $R_e <$ 1.1 pixels, which is 2σ above the mean of the distribution in Fig. 8. A number of point sources remain in the catalogue, in particular some bright, saturated stars whose wings give a larger R_e. Following visual inspection of our images, we estimate that <2 per cent of the objects in our sample are unresolved, these are a mixture of unrejected stars, and unresolved objects such as Coma cluster ultra-compact dwarfs.

6.2 Magnitude–surface brightness relation

Although we explicitly exclude any physical analysis of the structural catalogue in the present paper, we give a flavour of the types of objects included in the catalogue by showing (Fig. 12) a plot of

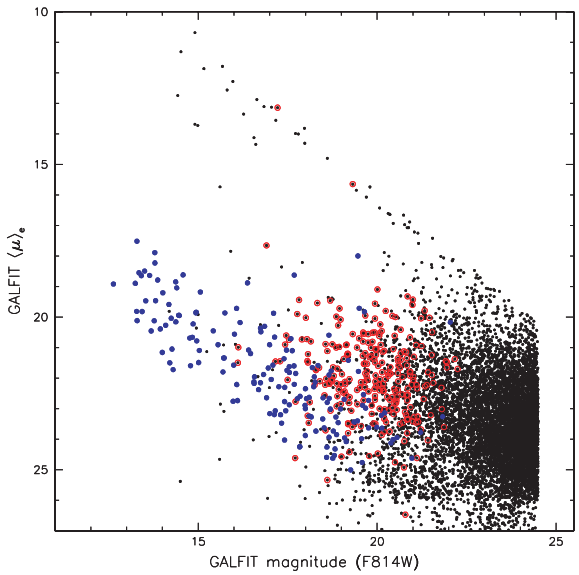

Figure 12. $\langle\mu\rangle_e$ plotted against $F814W$ magnitude for the objects in the catalogue. The larger blue points are spectroscopically confirmed cluster members, black dots surrounded by red circles are spectroscopically confirmed not to be members. Small black dots without a red circle are objects with no measured redshift. The diagonal line of black dots at upper right is the remaining, partly saturated, stellar contamination.

$\langle\mu\rangle_e$ against magnitude, measured with GALFIT, for the objects in the catalogue. In this plot, blue denotes confirmed cluster members (from the redshifts of Marzke et al., in preparation), red circles confirmed non-members and the black dots objects without measured redshifts.

There is a diagonal line of black (and a few red) points at the upper right, this is the residual stellar contamination, in the case of the bright points these stars are saturated in the ACS images, and hence have measured $R_e > 1.1$ pixels. The cluster members form a sequence towards the lower left, with a positive correlation between $\langle\mu\rangle_e$ and luminosity. This sequence has considerable scatter as the galaxies have not been selected by morphological type nor n. Confirmed non-members (almost all background) have in general higher surface brightness for their apparent magnitude; however, there are also cluster members with brighter $\langle\mu\rangle_e$. These are compact ellipticals similar to those discussed by Price et al. (2009).

6.3 External comparison

Gutiérrez et al. (2004) and Aguerri et al.(2005) study the structural parameters of dwarf galaxies in the Coma cluster using ground-based data obtained with the Isaac Newton Telescope at La Palma, in the Sloan-r filter. Some of the decompositions in these papers fit multiple components; here we only focus on the galaxies which have bulge-to-total ratios B/T $\geqslant 0.8$ in the Gutiérrez et al. sample and the dEs (excluding the dS0s) from the Aguerri et al. sample. 17 galaxies from Gutiérrez et al. and seven galaxies from Aguerri et al. match within 2.0 arcsec with galaxies in our structural catalogue. In Fig. 13 we present a comparison between the effective radii R_e and μ_e, the surface brightness at R_e, for these galaxies. The correlation is good, with a few outliers, mostly galaxies with complex structures in their centres which are not well resolved in the ground-based data.

7 COMPARISON BETWEEN GIM2D AND GALFIT

Both the GIM2D and GALFIT simulations have shown that these two codes are capable of recovering parameters of simulated galaxies in an almost unbiased way down to very low S/N values. However, galaxies seldom consist of a single Sérsic component. This makes a comparison between GALFIT and GIM2D for real sources interesting. Even though both codes try to minimize a figure-of-merit (a χ^2 value), there are significant differences in both the way this minimization is achieved (Markov Chain Monte Carlo versus Levenberg–Marquardt minimization) and how the best-fitting parameters are determined (median value of a number of realizations in the case of GIM2D versus final value after a number of iterations in the case of GALFIT). These differences could, in principle, have an impact on the performance of both codes even in the case of objects satisfying the magnitude, $\langle\mu\rangle_e$ and R_e cuts described in Section 6.

7.1 Comparison of the fitted values

The top two quadrants of Fig. 14 show the difference between the measured magnitudes, effective radii and Sérsic indices plotted against the measured $F814W$ magnitude. Quadrant (a) presents the results for objects with a measured Sérsic index lower than 2.5, whilst quadrant (b) presents the results for objects of higher Sérsic indices. Quadrants (c) and (d) of this figure present these differences plotted against the $F814W$ $\langle\mu\rangle_e$ for the same division in Sérsic index. The objects included in these plots are a subset of the full catalogue

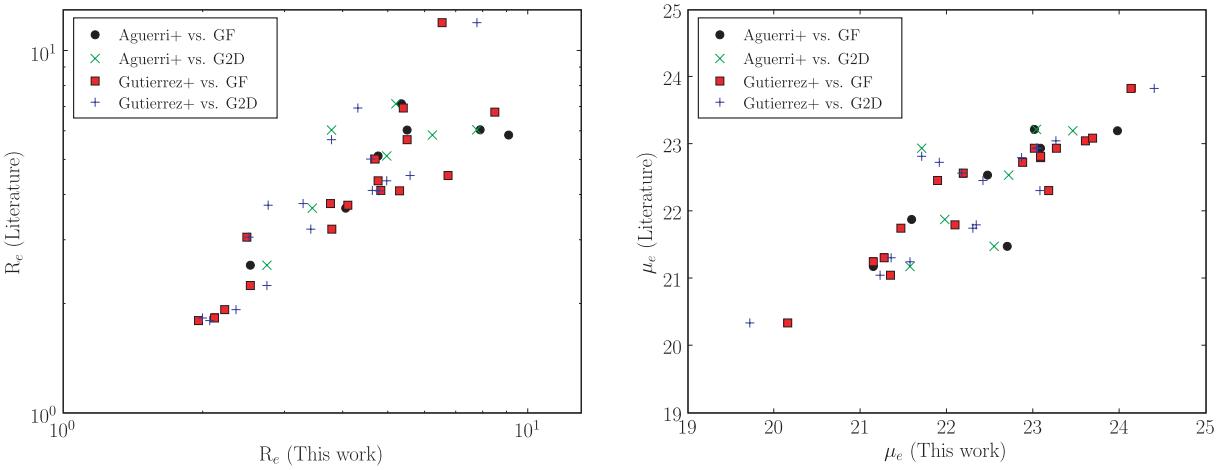

Figure 13. Comparison of our derived structural parameters with those of Aguerri et al. (2005) and Gutiérrez et al. (2004). Left-hand panel: R_e in arcseconds; Right-hand panel: μ_e. Filled symbols represent our GALFIT values and crosses our GIM2D values, as described in the legend at upper left in each panel.

described in Section 6. The additional constraints for inclusion in these plots are

(i) $\langle\mu\rangle_e \leqslant 24.5$
(ii) RFF $\leqslant 0.11$ and EVI $\leqslant 0.95$
(iii) $0.5 < n < 8.0$.

In each case the galaxies had to satisfy the constraint for both codes. These additional cuts guarantee that the objects included in these plots are well measured and well represented by Sérsic profiles.

These plots show that, whenever the two codes yield a Sérsic index lower than 2.5, the observed agreement between the output parameters is quite remarkable even for the Sérsic index itself. In this case, the expected magnitude scatter between the two codes is around 0.25 mag at the faintest levels, with a similar agreement in the R_e measurements.

Quadrants (b) and (d) of Fig. 14 show that in the cases in which the two codes measure a Sérsic index higher than 2.5, the disagreement between the two codes is larger. It is therefore more difficult to get consistent measurements for objects with extended wings containing a large fraction of the object's flux. This disagreement between the two codes manifests itself not only as a larger scatter, but also as a systematic trend of the effective radii and Sérsic index residuals, when plotted against the measured surface brightnesses.

Whenever one code finds a brighter magnitude than the other, it also finds R_e to be larger. This is in agreement with Fig. 3. This is probably caused by differences in the sky values adopted by the two codes. This is also the probable cause of the poorer agreement between the two codes when fitting objects with high Sérsic indices. For these objects, and in particular for sources that are found to be in the luminous haloes of the largest galaxies, it is very difficult to define the sky level with accuracy simply because these sources have a large fraction of their total flux in very extended wings and thus, any small discrepancy in the measured sky level translates into a large difference in the final luminosity and effective radius.

Fig. 14 also shows that the scatter in the output Sérsic index is larger for higher values of this index. This is caused by the fact that models of high Sérsic index start to converge towards a limiting r^{-2} profile and it is therefore very difficult to distinguish between two such models.

Another discrepancy between the two codes comes from small sources. Often these sources are fitted by GALFIT with a very high Sersíc index and a half-light radius of a few pixels. These fits have a substantial portion of their light in wings which are below the detection threshold. On the other hand, GIM2D fits these sources with lower Sérsic indices, and the GIM2D fit is probably a more realistic representation of the detected image.

One advantage of GALFIT is that it can model a number of galaxies simultaneously, leading to more consistent fits in cases where the target galaxy has near neighbours. GIM2D sometimes has problems with these sources as the only thing GIM2D can do with neighbouring sources is to mask them, and that fraction of the flux from these neighbouring sources which falls outside of their masks will compromise the fits.

8 SUMMARY, CONCLUSIONS AND FUTURE WORK

We have fitted single Sérsic models to the surface brightness distributions of 74 992 galaxies included in the photometric catalogue presented in Paper II, using the two most widely used two-dimensional galaxy fitting codes, GIM2D and GALFIT. Both codes create a PSF convolved trial function which is then compared to the input science data. The PSFs used were created mimicking the most important reduction steps that the science images had undergone.

Independent simulations show that both codes can achieve similar accuracies for most cases. However, GIM2D requires a much higher degree of intervention compared with GALFIT to produce the results. This is due to the greater flexibility of GALFIT, which makes it easier for any given input image to satisfy the fitting hypothesis under which GALFIT works. GIM2D needs more manual work, including the use of enlarged masks with sizes calculated according to our detailed SEXTRACTOR simulations, and the masking of nearby sources, to produce reliable results.

These simulations, together with an additional constraint aimed at rejecting probable point sources, have been used to select a subsample of galaxies from the initial SEXTRACTOR catalogue. The criteria used are

(i) $\langle\mu\rangle_e < 26.0$, where $\langle\mu\rangle_e$ is the mean surface brightness enclosed within R_e,
(ii) $F814W < 24.5$,
(iii) $R_e > 1.1$ pixels.

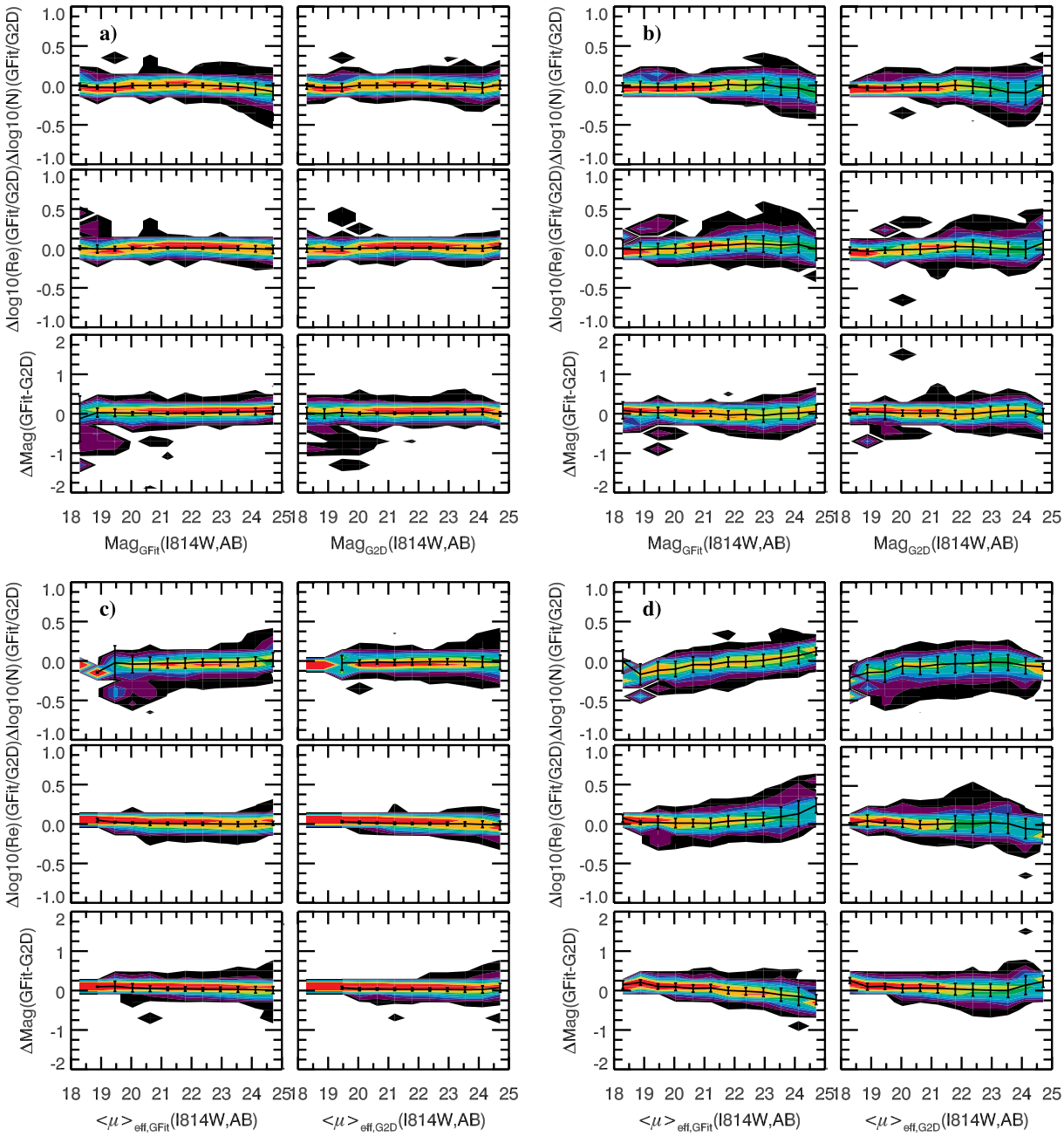

Figure 14. Quadrant (a): magnitude, effective radius and Sérsic index residuals as a function of GALFIT magnitude (left-hand panels) and GIM2D magnitude (right-hand panels). This quadrant shows results for galaxies with $n < 2.5$. Quadrant (b): same for objects with $n > 2.5$. Quadrant (c): magnitude, effective radius and Sérsic index residuals as a function of GALFIT $\langle\mu\rangle_e$ (left-hand panels) and GIM2D $\langle\mu\rangle_e$ (right-hand panels). This quadrant shows results for galaxies with $n < 2.5$. Quadrant (d): same for objects with $n > 2.5$. Details of the vertical error bars and colour coding, are as in Fig. 4.

We find that 8814 objects satisfy these criteria, cross-matching with the redshift catalogue of Marzke et al. (in preparation), indicates that 424 of these have redshifts, of which 163 have redshifts which place them as probable cluster members.

We have also introduced two different goodness-of-fit diagnostics. The RFF is an indicator of the amount of light contained in the residuals which cannot be accounted for by the per-pixel photometric errors associated with the science image. The EVI measures the importance of the internal structure present in luminous galaxies that the Sérsic model is unable to reproduce. These diagnostics indicate whether the surface brightness distributions of the fitted galaxies are well described by the Sérsic profiles, or alternatively whether it is valuable to use more complex functional forms (maybe adding a nuclear point source, or a bulge+disc decomposition) than the simple Sérsic profile used in this work.

Although the Sérsic fits presented here provide a good overall description of the majority of galaxies in our sample, the spatial resolution and stability of the PSF provided by *HST* and ACS allow the surface brightness to be measured accurately over a wide dynamic range. A range of more complex functions have been fit

to surface brightness profiles, such as the 'dual power law' (Ferrarese et al. 1994), the 'Nuker Law' (Lauer et al. 1995) and the core-Sérsic profile (Graham et al. 2003; Trujillo et al. 2004). In the context of elliptical and spheroidal galaxies, a number of authors (e.g. Graham & Guzmán 2003; Graham 2004; Merritt & Milosavljević 2005; Ferrarese et al. 2006; Côté et al. 2007; Kormendy et al. 2009), have identified and measured either 'extra light' or 'missing light' with respect to the Sérsic formalism in their profiles. In future papers, in this series we will investigate in detail these deviations from the Sérsic profile, and the correlation with kinematic properties (Skillman & Haynes 2004; Cappellari et al. 2007; Emsellem et al. 2007; Krajnović et al. 2008, van Zee, Toloba et al. 2009).

An alternative formalism which we will test for surface brightness profiles of ellipticals derives from the modified isothermal models of King (1962, 1966) and Wilson (1975), which are very successful in reproducing the surface brightness distributions of star clusters, and of some, but not all, elliptical galaxies.

In the current paper, we analyse only the radial surface brightness profile, but there is also information in the azimuthal distribution, and we will undertake decompositions into disc, bulge and nuclear components where appropriate (Andredakis et al. 1995; Balcells et al. 2007a,b), which will permit the construction of more meaningful structural parameter diagrams for the different physical components.

We will also investigate asymmetric deviations from the basic Sérsic formulation of the light distribution, using techniques for parametrizing galaxy surface brightness such as CAS (Conselice 2003) and Gini/M20 (Lotz, Primack & Madau 2004), and for detecting and quantifying bars (Marinova et al. 2010).

ACKNOWLEDGMENTS

We thank Dr Luc Simard for providing the code DrizzlyTim. DC and AMK acknowledge support from the Science and Technology Facilities Council, under grant PP/E/001149/1. CH acknowledges financial support from the Estallidos de Formación Estelar. Fase III, under grant AYA 2007-67965-C03-03/MEC. MB acknowledges financial support from grants AYA2006-12955 and AYA2009-11137 from the Spanish Ministerio de Ciencia e Innovación. DM was supported by grants AST-0807910 (NSF) and NNX07AH15G (NASA).

REFERENCES

Aguerri J. A. L., Iglesias-Páramo J., Vílchez J. M., Muñoz-Tuñón C., Sánchez-Janssen R., 2005, AJ, 130, 475
Andredakis Y. C., Peletier R. F., Balcells M., 1995, MNRAS, 275, 874
Balcells M., Graham A. W., Domínguez-Palmero L., Peletier R. F., 2003, ApJ, 582, L79
Balcells M., Graham A. W., Peletier R. F., 2007a, ApJ, 665, 1084
Balcells M., Graham A. W., Peletier R. F., 2007b, ApJ, 665, 1104
Bertin E., Arnouts S., 1996, A&AS, 117, 393
Blakeslee J. et al., 2006, ApJ, 644, 30
Caon N., Capaccioli M., D'Onofrio M., 1993, MNRAS, 265, 1013
Capaccioli M., 1989, in Corwin H. G., Bottinelli L., eds, The World of Galaxies. Springer-Verlag, Berlin, p. 208
Cappellari M. et al., 2007, MNRAS, 379, 418
Carter D. et al., 2008, ApJS, 176, 424 (Paper I)
Chiboucas K., Tully R. B., Marzke R. O., Trentham N., Ferguson H. C., Hammer D., Carter D., Khosroshahi H. G., 2010a, ApJ, 723, 251
Chiboucas K. et al., 2010b, ApJ, in press (arXiv:1009.3950)
Colless M. M., Dunn A. M., 1996, ApJ, 458, 435
Conselice C. J., 2003, ApJS, 147, 1
Côté P. et al., 2007, ApJ, 671, 1456
de Vaucouleurs G., 1948, Ann. Astrophys., 11, 247
de Vaucouleurs G., 1957, AJ, 62, 69
de Vaucouleurs G., 1959, ApJ, 130, 728
Emsellem E. et al., 2007, MNRAS, 379, 401
Erwin P., Beckman J. E., Pohlen M., 2005, ApJ, 626, L81
Ferrarese L., van den Bosch F. C., Ford H. C., Jaffe W., O'Connell R. W., 1994, AJ, 108, 1598
Ferrarese L. et al., 2006, ApJS, 164, 334
Freeman K. C., 1970, ApJ, 160, 811
Graham A. W., 2004, ApJ, 613, L33
Graham A. W., Driver S. P., 2005, Publ. Astron. Soc. Australia, 22, 118
Graham A. W., Guzmán R., 2003, AJ, 125, 2936
Graham A. W., Worley C. C., 2008, MNRAS, 388, 1708
Graham A. W., Lauer T. R., Colless M., Postman M., 1996, ApJ, 465, 534
Graham A. W., Erwin P., Trujillo I., Asensio Ramos A., 2003, AJ, 125, 2951
Gray M. E. et al., 2009, MNRAS, 393, 1275
Gutiérrez C. M., Trujillo I., Aguerri J. A. L., Graham A. W., Caon N., 2004, ApJ, 602, 664
Hammer D. et al., 2010, ApJS, 191, 143 (Paper II)
Häussler B. et al., 2007, ApJS, 172, 615
Hubble E. P., 1930, ApJ, 71, 231
Jee M. J., Blakeslee J. P., Sirianni M., Martel A. R., White R. L., Ford H. C., 2007, PASP, 119, 1403
King I. R., 1962, AJ, 67, 471
King I. R., 1966, AJ, 71, 64
Koekemoer A. M., Fruchter A. S., Hook R. N., Hack W., 2003, in Arribas S., Koekemoer A., Whitmore B., eds, 2002 HST Calibration Workshop. STScI, Baltimore, p. 337
Kormendy J., Fisher, D B., Cornell, M E., Bender R., 2009, ApJS, 182, 216
Krajnović D. et al., 2008, MNRAS, 390, 93
Krist J., 1993, in Hanisch R. J., Brissenden R. J. V., Banes J., eds, ASP Conf. Ser. Vol. 52, Astronomical Data Analysis Software and Systems II. Astron. Soc. Pac., San Francisco, p. 536
Krist J., 2003, HST Interim Science Report 0306 (STScI)
Lauer T. R. et al., 1995, AJ, 110, 2622
Lotz J. M., Primack J., Madau P., 2004, AJ, 128, 163
Marinova I. et al., 2010, in Stanford L. M., Green J. D., Hao L., Mao Y., eds, ASP Conf. Ser. Vol. 432, New Horizons in Astronomy. Astron. Soc. Pac., San Francisco, p. 219
Marleau F. R., Simard L., 1998, ApJ, 507, 585
Merritt D., Milosavljeviç M., 2005, Living Rev. Relativity, 8, 8
Mobasher B. et al., 2001, ApJS, 137, 279
Moffat A. W. J., 1969, A&A, 3, 445
Patterson F. S., 1940, Harvard College Obser. Bull., 914, 9
Peng C. Y., Ho L. C., Impey C. D., Rix H.-W., 2002, AJ, 124, 266
Peng E. et al., 2010, ApJ, submitted
Price J. et al., 2009, MNRAS, 397, 1816
Reynolds J. H., 1913, MNRAS, 74, 132
Rhodes J. D. et al., 2007, ApJS, 172, 203
Rix H.-W. et al., 2004, ApJS, 152, 163
Sérsic J. L., 1963, Bol. Asoc. Argentina Astron., 6, 41
Sérsic J. L., 1968, Atlas de Galaxias Australes. Obser. Astron., Córdoba
Sikkema G., 2009, PhD thesis, Rijksuniversiteit Groningen
Simard L. et al., 2002, ApJS, 142, 1
Strazzullo V. et al., 2010, A&A, 524, A17
Toloba E. et al., 2009, ApJ, 707, L17
Trujillo I., Graham A. W., Caon N., 2001, MNRAS, 326, 869
Trujillo I., Erwin P., Asensio Ramos A., Graham A. W., 2004, AJ, 127, 1917
Trujillo I. et al., 2006, MNRAS, 373, L36
Valentijn E. A. et al., 2007, in Shaw R. A., Hill F., Bell D. J., eds, ASP Conf. Ser. Vol. 376, Astronomical Data Analysis Software and Systems XVI. Astron. Soc. Pac., San Francisco, p. 491
van der Kruit P. C., Searle L., 1981a, A&A, 95, 105
van der Kruit P. C., Searle L., 1981b, A&A, 95, 116
van der Wel A., Holden B. P., Zirm A. W., Franx M., Rettura A., Illingworth G. D., Ford H. C., 2008, ApJ, 688, 48
van Dokkum P. G., 2001, PASP, 113, 1420
van Zee L., Skillman E. D., Haynes M. P., 2004, AJ, 128, 121
Wilson C. P., 1975, AJ, 80, 175

APPENDIX A: COMPARISON TO GIM2D AND GALFIT RESULTS BY THE GEMS COLLABORATION

Wanting to build upon the experience obtained by other teams in using GALFIT and GIM2D on *HST*/ACS data, we decided that the best starting point is the extensive GALFIT/GIM2D comparison by the GEMS collaboration (Häussler et al. 2007) on mock *HST*/ACS observations. The GEMS collaboration provides public access to the analysis and actual data on the web (http://www.mpia.de/GEMS/fitting_paper.html). We used their Bulge0001 and Disk0001 simulated observations. These contain artificial galaxies with pure Sérsic profiles with $n = 4$ or 1, respectively, with appropriate Poisson noise, on top of a noise background created by putting together patches of real sky observations from different images. These simulated images are created for the *F*850*LP* filter using a PSF with an FWHM typical of this filter. The artificial galaxies cover a significant fraction of the galaxy parameter space expected for the Coma *HST*/ACS data, in terms of S/N, total magnitude and effective radius. Therefore our analysis of these data is useful even though the Coma Legacy Survey does not use the *F*850*LP* filter.

Following the work by Häussler et al. (2007), we fit a pure Sérsic model with a flat background. All the parameters, including the Sérsic index, were allowed to vary freely, although the value of the residual sky was later fixed, as explained below. The PSF used was identical to the one used to create the mock galaxies.

For GALFIT, we converged on a very similar fitting set-up and best-fitting results as Häussler et al.. For GIM2D, we arrived at a different set-up and masking treatment which led to improvements in the best-fitting results.

First, GIM2D was run with its default decision algorithm on the size of the cutout to be fitted. It was also allowed to fit and refine the sky value by itself (DOBKG = YES) and to automatically estimate initial values for the fitted parameters (INITPARAM = YES). The Sérsic index was left as a free floating parameter. The SExtractor parameter configuration ensures detection of sources with a global S/N of 20.25. The SExtractor parameter BACK SIZE was set to 512. The minimum stamp size was set to 31 pixel. This experimental configuration leads to the 'recommended' set-up for GIM2D. The noise model used for the GIM2D fits was based on the traditional CCD equation using the background σ and the image effective gain which is ultimately regulated by the exposure time and reduction process.

For the Disk0001 models, GIM2D produced a fit for 470 simulated profiles. Fig. A1 shows the results obtained by GIM2D in this case. The upper panel presents the magnitude residuals, the middle panel presents the ratio in effective radii, and the lower panel presents the output Sérsic index as a function of the average surface brightness within a effective radius of the simulation. Our GIM2D results are shown by red crosses and the GEMS team results with GIM2D by the blue circles. The general conclusion from this is that there are systematic trends at the faintest surface brightness levels, fainter than $\langle\mu\rangle_e \geqslant 22.5$. The scatter between fit and simulation is smaller for our GIM2D run compared with the results of the GEMS team. Likely, this is caused by the fact that we masked overlapping sources with a value of -2 in the mask image, a situation that forces GIM2D to ignore those problematic pixels. The GEMS group did not do this.

For the Bulge0001 models, GIM2D yielded a successful fit for 558 simulations. Fig. A2 shows the results. The general conclusion is that our results are an improvement on the GEMS results down to a surface brightness of around $z \sim 22.5$, and have a smaller scatter. However there are again systematic trends which increase with fainter surface brightness.

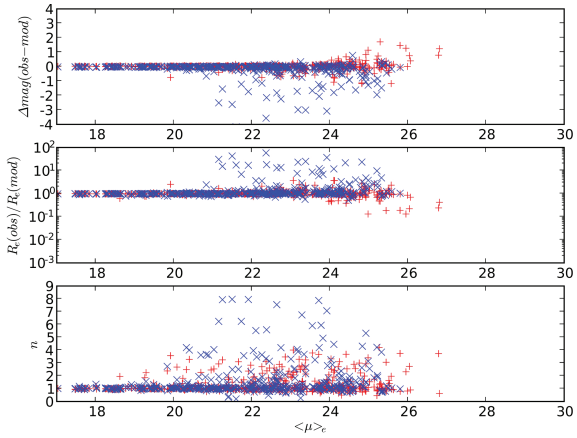

Figure A1. Results for GIM2D on pure exponential models. From top to bottom: magnitude residual (GIM2D minus model), ratio of effective radius (GIM2D / model) and Sérsic index as a function of the true average surface brightness within an effective radius. Red (horizontal) crosses are our GIMD2D runs, blue (diagonal) crosses are the results for the same simulated galaxies from the GEMS team.

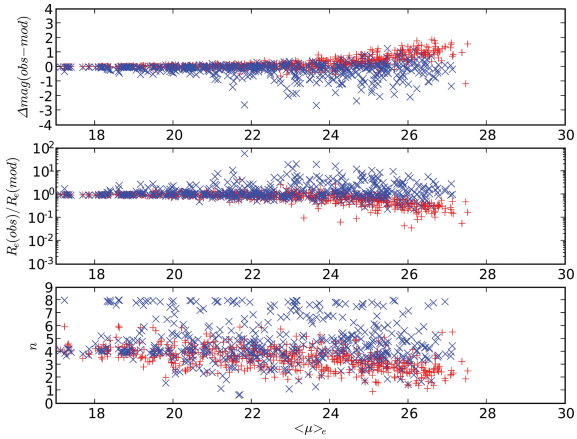

Figure A2. Results for GIM2D on pure de Vaucouleurs models. From top to bottom: magnitude residual (GIM2D minus model), ratio of effective radius (GIM2D / model) and Sérsic index as a function of the true average surface brightness within an effective radius. Red (horizontal) crosses are our GIMD2D runs, blue (diagonal) crosses are the results for the same simulated galaxies from the GEMS team.

We investigated if the systematic deviations shown by the GIM2D solutions at surface brightness levels fainter than $z = 23.0$ could be due to an inaccurate sky. To this end a number of low surface brightness sources were refit. This time, we used a sky determination derived from a customized configuration file for SExtractor whose main difference with the SExtractor configuration file used in the previous fitting round is that it uses a 2048 mesh for background subtraction and determination. Also, we did not allow GIM2D to fit the sky. Furthermore the cutout size for GIM2D was increased to 25 times the default size.

Fig. A3 shows the result of this test for the mock galaxies present in image Disk0001. Comparison with Fig. A1 shows that, using this prescription to deal with the sky level, GIM2D no longer shows systematic offsets in magnitudes and effective radius even at the faintest surface brightness levels.

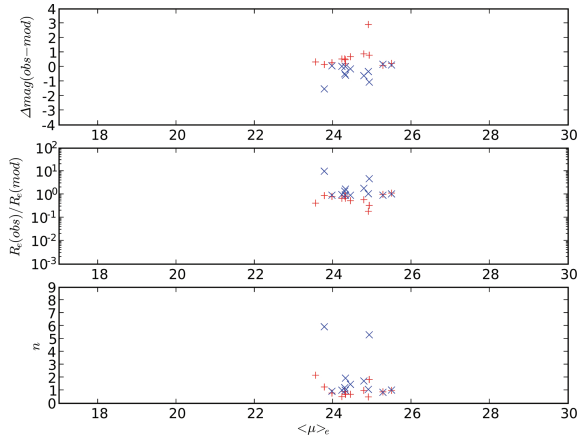

Figure A3. Results for GIM2D on pure exponential models of low surface brightness, using our own sky determination (see text). From top to bottom: magnitude residual (GIM2Dminus model), ratio of effective radius (GIM2D / model) and Sérsic index as a function of the true average surface brightness within an effective radius. Red (horizontal) crosses are our GIMD2D runs, blue (diagonal) crosses are the results for the same simulated galaxies from the GEMS team.

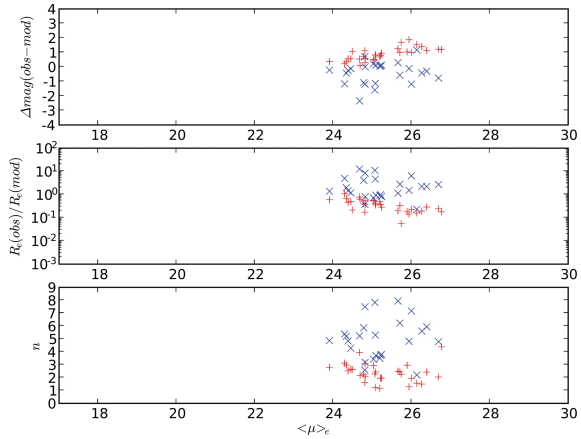

Figure A4. Results for GIM2D on pure de Vaucouleurs models of low surface brightness, using our own sky determination (see text). From top to bottom: magnitude residual (GIM2D minus model), ratio of effective radius (GIM2D / model) and Sérsic index as a function of the true average surface brightness within an effective radius. Red (horizontal) crosses are our GIMD2D runs, blue (diagonal) crosses are the results for the same simulated galaxies from the GEMS team.

Fig. A4 shows the result of this fitting round for the models included in the Bulge0001 image. Comparison to Fig. A2 clearly shows that setting the sky to be equal to the sky value given by SExtractor makes the systematic offsets in magnitudes and effective radius to vanish even at the faintest surface brightness levels. The statistical errors (the scatter) are rather large however.

From the fits to the synthetic models generated by the GEMS team comprising either pure exponentials or pure de Vaucouleurs models, we conclude the following.

(i) The errors in the recovery of parameters appear to be dominated by errors in the sky determination.

(ii) Our G2D fits show significantly reduced scatter with respect to the G2D fits published by GEMS team. The difference can probably be traced to the manual masking of intervening sources in the object's mask done by our team.

(iii) Increasing the cutout size used by GIM2D reduces or removes the systematic offsets in magnitude and effective radius found when the default cutout size is used.

(iv) Overall, we conclude that we can use both the GALFIT and GIM2D codes with a similar or better accuracy to that found by the GEMS collaboration.

APPENDIX B: CREATING OBJECT MASKS FOR GIM2D

We provide a detailed recipe for producing object masks for GIM2D that solves the missing flux problem that appears when standard SExtractor segmentation masks are used in GIM2D.

(i) The aperture for the target should ideally be equal to the Kron aperture of an object with the same FLUX_RADIUS and n that would be measured if the observations had infinite S/N. The elongation and position angle of this aperture would ideally be equal to those of the real object. The pixels within this aperture should be flagged as 1 in the mask file so that GIM2D recognizes them as belonging to its target object. This aperture is calculated from the SExtractor measurements. FLUX_RADIUS, THETA_IMAGE and ELONGATION were taken directly from the SExtractor catalogue. MUOBS is a SExtractor based estimate of effective surface brightness of that particular detection, obtained as if MAG_AUTO were the total magnitude and the 50 per cent of FLUX_RADIUS were the real effective radius. It is thus an estimate of the effective surface brightness. The fifth-degree polynomials used in the SExtractor simulations presented in Paper II were then used to estimate empirically the effective radius of the source. This effective radius estimate is then converted into a Kron aperture using the relationship between R_e and R_1 (the S/N=∞ Kron aperture in units of the effective radius) and n. $n = 2.5$ is assumed, where n is undefined. Although the aperture defined in this way leaves out a finite fraction of the total flux from the target models outside the mask, this magnitude offset is 0.1 mag in the worst case. For this reason, the initial flux estimate will be around 0.1 mag fainter than the true integrated flux. As above, a very similar statement can be made about the initial effective radii estimates. Using this customized mask, GIM2D has a realistic opportunity to measure 100 per cent of the target object total flux and size, whereas with the default SExtractor segmentation image, this is not true.

(ii) The apertures for the background sources are elliptical apertures, with an area given by the ISOAREA_IMAGE SExtractor measurement. The elongation and position angles of these ellipses are also taken from the SExtractor measurements. These pixels are flagged as -2 so that GIM2D ignores these pixels in all calculations. GIM2D is therefore blind to the innermost regions of the background sources. Thus only the outer regions of the background sources contribute to the sky level affecting the galaxy under study. In the case of an overlap between target and background object pixels, the pixels are assigned to the background object as including them in the target would potentially compromise the fit.

(iii) Finally, pixels not belonging to the target or to the background sources are flagged as 0, so that GIM2D regards these pixels as sky.

In a few cases, for instance, with objects with close neighbours or near to the CCD edges, SExtractor did not provide measurements of MAG_AUTO and FLUX_RADIUS. In these cases MUOBS is estimated by spreading the light encircled in the isophotal area of the object (ISOAREA_IMAGE) uniformly in an aperture with a radius equal to $(1/2) \times \sqrt{\text{ISOAREA\_IMAGE}/\pi}$. This was found to

be somewhat brighter than a measured MUOBS, although the final apertures obtained were similar in size.

The size of the post-stage stamp over which GIM2D has to work is an integral part of the suggested solution. The quantity FRAD_MOD amounts, in the vast majority of the cases, to 50 per cent of FLUX_RADIUS, as calculated by SExtractor. For the objects where SExtractor could not calculate FLUX_RADIUS, FRAD_MOD is half of the radius of the circle with an area equal to ISOAREA_IMAGE, which always does exist.

The number YFX(MUOBS) is given by the empirical relation between the 50 per cent FLUX_RADIUS and the *input* effective radius that is appropriate for sources with a high n. For reasonable Sérsic indices, YFX(MUOBS) is given by the fifth-order polynomial in the mean observed surface brightness MUOBS, presented in Paper II. The final size of the post stamps imagelets extracted is $7.0 \times$ FRAD_MOD $\times$ YFX(MUOBS) on a side.

This paper has been typeset from a TEX/LATEX file prepared by the author.